Journal of Physics: Condensed Matter

PAPER

Dominant contributions to the apparent activation energy in two-dimensional submonolayer growth: comparison between Cu/Ni(111) and Ni/Cu(111)

To cite this article: Joseba Alberdi-Rodriguez *et al* 2020 *J. Phys.: Condens. Matter* **32** 445002

IOP Publishing
Journal of Physics: Condensed Matter
J. Phys.: Condens. Matter **32** (2020) 445002 (25pp)
https://doi.org/10.1088/1361-648X/ab9b50

Dominant contributions to the apparent activation energy in two-dimensional submonolayer growth: comparison between Cu/Ni(111) and Ni/Cu(111)

Joseba Alberdi-Rodriguez[1,2,3,5], **Shree Ram Acharya**[4], **Talat S Rahman**[1,4], **Andres Arnau**[1,2,3] **and Miguel A Gosálvez**[1,2,5]

[1] Donostia International Physics Center (DIPC), Manuel Lardizabal 4, 20018 Donostia-San Sebastián, Spain
[2] Departamento de Física de Materiales, University of the Basque Country UPV/EHU, Manuel Lardizabal 3, 20018 Donostia-San Sebastián, Spain
[3] Centro de Física de Materiales CFM-Materials Physics Center MPC, Centro mixto CSIC – UPV/EHU, Manuel Lardizabal 5 20018 Donostia-San Sebastián, Spain
[4] Department of Physics, University of Central Florida, Orlando, FL 32816, United States of America

E-mail: joseba.alberdi@ehu.eus and miguelangel.gosalvez@ehu.eus

Received 16 April 2020, revised 19 May 2020
Accepted for publication 10 June 2020
Published 7 August 2020

Abstract

For surface-mediated processes in general, such as epitaxial growth and heterogeneous catalysis, a constant slope in the Arrhenius diagram of the rate of interest, R, against inverse temperature, $\log R$ vs $1/T$, is traditionally interpreted as the existence of a bottleneck elementary reaction (or rate-determining step), whereby the constant slope (or apparent activation energy, E^R_{app}) reflects the value of the energy barrier for that elementary reaction. In this study, we express E^R_{app} as a weighted average, where every term contains the traditional energy barrier for the corresponding elementary reaction plus an additional configurational term, while identifying each weight as the probability of executing the corresponding elementary reaction. Accordingly, the change in the leading (most probable) elementary reaction with the experimental conditions (e.g. temperature) is automatically captured and it is shown that a constant value of E^R_{app} is possible even if control shifts from one elementary reaction to another. To aid the presentation, we consider kinetic Monte Carlo simulations of submonolayer growth of Cu on Ni(111) and Ni on Cu(111) at constant deposition flux, including a large variety of single-atom, multi-atom and complete-island diffusion events. In addition to analysing the dominant contributions to the diffusion constant of the complete adparticle system (or tracer diffusivity) and its apparent activation energy as a function of both coverage and temperature for the two heteroepitaxial systems, their surface morphologies and island densities are also compared.

Keywords: apparent activation energy, epitaxial growth, surface morphology, island diffusion, kinetic Monte Carlo

(Some figures may appear in colour only in the online journal)

---

[5] Authors to whom any correspondence should be addressed.

1. Introduction

Two-dimensional (2D) materials have attracted interest due to their superior properties and promising applications [1–7]. However, their future success depends on the ability to achieve large-scale production of high-quality samples via a variety of surface-mediated processes [1]. As an example, the synthesis of 2D organic networks is well established, based on both molecular self assembly (MSA) and on-surface synthesis (OSS) [8, 9]. While MSA refers to the spontaneous arrangement of molecular units into ordered structures controlled by weak interactions, such as van der Waals forces and/or hydrogen (or halogen) bonding, OSS relates to reactions that occur only on surfaces, leading to new compounds unachievable by other means, e.g. Ullmann-type reactions of halogen terminated molecular precursors for the synthesis of polymeric chains through the onset of intermolecular covalent-bonds. Similarly, traditional surface-mediated growth techniques, such as chemical vapour deposition (CVD), are nowadays used for the synthesis of 2D materials, such as graphene, molybdenum disulfide (MoS_2), etc [10–17]. Relying on thermal activation, a common feature of all previous techniques is that the adparticles diffuse randomly, eventually forming small clusters at random locations (nucleation), which gradually evolve into larger structures (e.g. complex flakes, compact islands, etc.) through the attachment of other diffusing adparticles (growth), which may eventually merge to form a single 2D layer (coalescence), provided the monomer supply is continued indefinitely. Most importantly, the quality of the resulting 2D material is affected markedly by the number and structure of the grain boundaries, directly depending on the actual size and shape of the domains (dendritic, compact, polygonal, etc), ultimately depending on the relative occurrence of the various diffusion events. Thus, the understanding of fundamental phenomena taking place via thermally-activated, collective diffusion on surfaces remains relevant for the production of high-quality samples of 2D materials.

Traditionally, low-energy electron diffraction (LEED) [18–20], field ion microscopy (FIM) [21, 22], scanning tunnelling microscopy (STM) [23] and related microscopies have enabled the observation of single molecules and atoms on the surface, thus providing specific insights regarding the growth process [24–28]. Nevertheless, also the theoretical interpretation and simulation of these images has contributed to the understanding of the molecular interaction, adsorption diffusion, assembly, and activation of precursors. Among these, we consider the kinetic Monte Carlo (KMC) method [29, 30], whose inherent spatial representation provides access to a wide variety of surface configurations, thus overcoming the mean-field limitation of traditional kinetics (in the standard 'well-mixed', homogeneous approximation [31]). In addition, KMC avoids monitoring the vibrational motion of every atom around its equilibrium position, as opposed to molecular dynamics (MD) [32], simply recognising that the important events (which modify the configuration of the system beyond the ubiquitous vibrational motion) correspond to the elementary reactions, such as adsorption, desorption, diffusion and recombination reactions, each occurring with a characteristic wait time (or rate constant). By ignoring the description of every vibration, the time increment in KMC is much larger than in MD, thus enabling much longer simulation times.

Due to the general role of diffusion in surface-mediated synthesis, here we study certain global features by focussing on the temperature dependence of submonolayer heteroepitaxial growth of metals under a temperature independent deposition flux F [33–37]. In particular, we are interested in analysing which diffusion events provide the most significant contributions to the overall diffusion constant (or diffusivity) when considering a wide variety of single-atom, multi-atom and complete-island diffusion events. Our method provides a general framework to determine the probability of observing any desired event type, corresponding to the frequency of execution of that event type normalised to the total frequency of execution of all event types. This is based on the observation that, for any given configuration of the surface, the frequency of execution of an event type is simply its total rate, which we describe as the product of its rate constant and its multiplicity, i.e. the abundance of that event type in the given surface configuration. Compared to previous approaches focussed on monitoring the execution of all event types [38], the use of the multiplicities offers an alternative route for the determination of the actual numbers of executed events. Most importantly, we show that an examination of the temperature dependence of the multiplicities enables resolving unambiguously the dominant contributions to the apparent activation energy of the diffusivity.

To test the proposed framework, we consider the growth of two heteroepitaxial systems, namely, Cu on Ni(111) and Ni on Cu(111), where the compact and stable (111) surfaces provide a small lattice mismatch with respect to the growing 2D islands ($\sim 2.5\%$), thus facilitating surface diffusion and enabling the achievement of concerted events, i.e. the diffusion of more than one adatom at once. Previous work includes theoretical studies on the diffusivity of small Cu islands on the Ni(111) surface [38] and of single Ni on the Cu(111) surface [39], as well as experimental reports on the growth of Cu/Ni(111) [40] (including a density functional theoretical study [41]) and Ni/Cu(111) [42–44]. By including the most important processes identified for the diffusion of small islands [38], we obtain a general picture on the relative importance of concerted diffusion in two-dimensional material growth, applied to metals.

The rest of the paper is organised as follows. Section 2 provides the computational and theoretical background. In particular, sections 2.1 and 2.2 describe the different diffusion events considered in the study, including single-atom, multi-atom and complete-island diffusion events as well as their energy barriers for the two chosen systems, namely, Cu on Ni(111) and Ni on Cu(111). This is followed by section 2.3, which presents the direct relation that exists between the diffusivity and the total diffusion rate, which in turn depends in a simple manner on the multiplicities of the various diffusion events. Then follows section 2.4, in which the multiplicities are used in order to define the probability of observing an event type, and section 2.5, which describes the apparent activation energy of the diffusivity by incorporating the temperature dependence of the multiplicities. Next, sections 3.1–3.4 present the results of the study, comparing the temperature dependence of the island density, morphology, total diffusion rate and its apparent activation energy for the two chosen systems. Finally, section 4 summarises the conclusions of the study.

2. Computational and theoretical aspects

2.1. Identification of diffusion events

The diffusion of adsorbates on a substrate is an essential part of film growth. In general, a diffusion event may consist of a single-atom hop (single-atom diffusion), a complete-island hop (concerted island diffusion) or a multi-atom hop at the perimeter of a compact island (concerted multi-atom diffusion) [45–51]. Here, an island is considered as a structure in which each atom is connected with at least one nearest neighbour. Based on an extensive study of post-adsorption diffusion kinetics of small islands of Cu/Ni(111) and Ni/Cu(111) as a function of the island size [38, 52], it was concluded that, in addition to single-atom diffusion, the most executed diffusive events consist of concerted diffusion of complete islands in the case of Ni/Cu(111), while in the Cu/Ni(111) system competition exists between concerted diffusion events and multi-atom events. That study considered island sizes up to eight atoms and concerted two-atom diffusion along the step-edge of compact islands. The current study includes these particular diffusion events.

The crystallographic structure of the fcc(111) surface under consideration in the simulations of this study is described by a triangular lattice. In this triangular lattice every node represents an adsorption site, so that we consider all adsorption sites at the nearest neighbour distance apart, which refers to either fcc or hcp sites of the surface. Any site is assigned a type (the unique combination of a class and a subclass), regardless of being occupied by an atom or not. The site class directly indicates the number of occupied nearest neighbour sites, and the subclass is simply a label that distinguishes between the different geometrical arrangements of the occupied neighboring sites (it points out how far the neighbours are from each other and it does not have any physical meaning). As shown in figure 1, we consider 7 site classes (from 0 to 6) and a maximum of 3 subclasses (from 0 to 2), leading to a total of 13 site types. The subclass is always 0 for classes 0, 1, 5 and 6, while it is arbitrarily and consistently assigned the value 0, 1 or 2 for classes 2, 3 and 4, depending on the geometrical arrangement.

For any particular diffusion event, the destination site is assigned the site type by considering that the atom has already hopped on it. Thus, for a destination site, the class and subclass are determined by considering the origin site as being empty. This is shown in figure 2. For the first column, the destination site will have no occupied neighbours and, thus, the type is 0 (class 0, subclass 0); for the second column, the destination site will have one occupied neighbour and, therefore, the type is 1 (class 1, subclass 0); and so on. Note that, in practice, there are only 12 origin types (0 to 11), since diffusion is impossible from type 12 (class 6, subtype 0). Furthermore, regarding the destination types, we consider some additional cases in order to take into account detachment events. Here, detachment means that the destination site has no neighbours in common with the origin site. This leads to a total of 16 destination types, as shown in figure B1 of the appendix. Consequently, we work with a transition table of 12 × 16 entries, where the rows correspond to the origin site types and the columns to the destination site types.

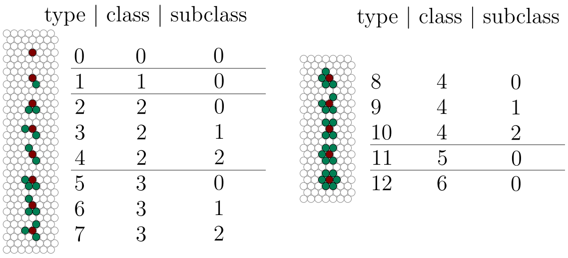

type	class	subclass
0	0	0
1	1	0
2	2	0
3	2	1
4	2	2
5	3	0
6	3	1
7	3	2
8	4	0
9	4	1
10	4	2
11	5	0
12	6	0

Figure 1. Site types considered in this study, indicated for the central site (in red). The type is a unique combination of class and subclass. The class directly indicates the number of occupied nearest neighbour sites (in green). The subclass is a label used to distinguish between different geometrical arrangements of the occupied neighbours.

In order to assign a type to a diffusion event, we use the origin and destination types of the involved sites. Some representative single-atom diffusion events are shown in figure 2 in which the atom at the origin site (in red) is moved one site to the right in each of the 14 examples. In this manner, monomer diffusion is described by a hop from type 0 to type 0 ($D[0,0] \rightarrow [0,0]$), while edge diffusion is described by a hop from type 2 to type 3 ($D\,[2,0] \rightarrow [2,0]$). Note that some transitions are physically impossible and, thus, not displayed. Similarly, we do not display the symmetry equivalent transitions for the other five hop directions (there are 6 possible directions in a triangular lattice), since all directions are treated identically.

In addition to single atom hops, we include concerted diffusion of islands, containing up to 8 atoms, where all the atoms belonging to the island move together in one of the six directions, independently of the island shape. For the calculation of the corresponding energy barrier (see section 2.2) the most compact shapes are used, as shown in figure 3(a). For instance, this means that all different trimer shapes have the same rate to move in any direction. Finally, we also include concerted two-atom diffusion along the perimeter of compact islands according to the four different event types shown in figure 3(b). Overall, we consider 118 different diffusion event types: 107 single-atom diffusion (figure B1 of the appendix), 7 complete-island moves (figure 3(a)) and 4 multi-atom hops (figure 3(b)).

2.2. Calculation of energy barriers and rates

Based on a many-body semi-empirical embedded-atom model (EAM) for the description of the interaction between the atoms [53], the diffusion energy barriers, E_{α}^{k}, required to compute the rate of each distinct diffusion event, are obtained by using the drag method [52, 54]. The EAM + drag combination produces

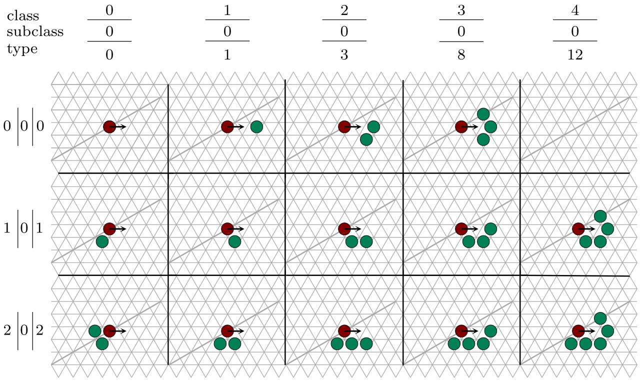

Figure 2. An extract of the total transition table for single-atom diffusion on a triangular lattice, showing a few representative origin site types (rows) and destination site types (columns). In all cases the red particle moves one lattice site to the right. The complete table appears in figure B1 of the appendix.

qualitative and semi-quantitative results with minor errors for metallic systems when compared with *ab initio* energetics, including island diffusion barriers on fcc(111) [38, 54]. For the calculations of barriers, the substrate consists of five fcc(111) layers with $16 \times 16 = 256$ atoms per layer, where the two bottom layers are kept frozen (to mimic the bulk) while the three top layers are allowed to relax. For each diffusion event, the required adatoms are placed on the surface on the desired initial configuration and the system is relaxed using standard MD cooling with velocity updates using the leap-frog algorithm, until the energy change between successive updates is less than 10^{-4} eV, taking the corresponding minimised energy as reference for the calculation of E^k_α.

In order to determine the energy barrier for a single-atom diffusion event, the chosen adatom is gradually dragged in steps of 0.05 Å along the reaction coordinate, whose direction is re-defined at every step as the vector from the relaxed location of the adatom to the aimed location in the final configuration. At every step, relaxation is allowed for the dragged adatom along the plane perpendicular to the current direction of the reaction coordinate while keeping fixed all other adatoms, the two bottom layers and the reaction coordinate, until the energy difference is less than 10^{-3} eV (1 meV) or the relaxed adatom is 0.05 Å from the aimed location. The maximum energy point in the energy profile of the minimum energy path represents the saddle point and its energy difference from the reference energy gives E^k_α for the diffusion event. For the configurations where some adatoms leave their assigned site upon relaxation, those adatoms are fixed. For multi-atom and concerted diffusion events, the same procedure is applied to the adatoms under consideration. See reference [52] for further details.

The computed energy barriers are displayed in tables B1 and B2 of the appendix. The barriers for monomer diffusion are within the expected range, compared with the literature [24]. Our diffusion barrier of 52 meV for Cu on Ni(111) is virtually the same as the previously reported value of 50 meV [55]. For diffusion of Ni on Cu(111), we obtain 31 meV, which is about 2/3 of the value (45 meV) reported in reference [55].

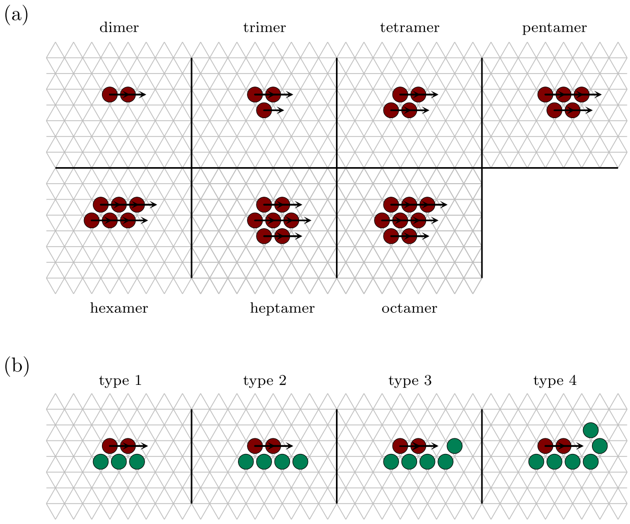

Figure 3. (a) Compact islands containing up to 8 atoms, used for the calculation of the diffusion energy barrier for complete-island diffusion. (b) Concerted diffusion events for two-atoms (in red) at the perimeter of an island (in green), classified according to the destination site type for the rightmost diffusing atom.

Once the energy barrier E^k_α has been obtained for diffusion event α, the corresponding diffusion rate (k_α) is computed by using equation A.1 (see appendix A.1).

2.3. Tracer diffusivity and total hop rate

Our theoretical analysis of the dominant contributions to the diffusion constant (or tracer diffusivity), D_T, is based on the fact that D_T is proportional to the total diffusion rate, R_d (see appendices A.1 and A.2):

$$D_\mathrm{T} = \frac{l^2}{2\delta\theta} f_\mathrm{T} R_d, \tag{1}$$

$$R_d = \sum_{\alpha \in \{d\}} M_\alpha k_\alpha. \tag{2}$$

In equation (1), l is the hop distance between adjacent adsorption sites; δ is the dimensionality (= 2 for diffusion on a surface); θ is the ensemble average of the coverage, determined by averaging the instantaneous coverage achieved at time t on many samples; and f_T is the correlation factor, defined as the proportionality factor between the ensemble average of the total square distance travelled by all the adparticles at time t and the ensemble average of the total number of performed diffusion hops also at time t (see appendix A.2). Typically, the temperature dependence of f_T is weak [33] and the use in this study of the same deposition flux at all temperatures (as in previous reports [33–37]) means that θ is independent of temperature (see appendix A.1 for further details). Overall, the temperature dependence of the diffusivity D_T is essentially contained in the total diffusion rate R_d. Thus, in this study we focus on monitoring the contributions to R_d as an excellent estimate of D_T.

In equation (2), $\{d\}$ denotes the collection of all distinct diffusion events and $\alpha \in \{d\}$ means that the summation is over all different hop rate constants. Accordingly, equation (2) means that the total diffusion rate, R_d, can be determined by summing over all different diffusion rate constants, k_α, each multiplied by the corresponding multiplicity, M_α, i.e. the abundance of that event type on the surface. Technically, both R_d and M_α are averaged quantities at three different levels: (i) according to the time dependence (time average), (ii) according to many samples (ensemble average), and (iii) per adsorption site (see appendices A.1 and A.2). We stress that the derivation of equation (1) contains no assumption on the particular geometry of the lattice, thus it is valid for triangular and square lattices. In general, one can write $M_\alpha = n_\alpha m_\alpha$, where n_α is the density of those particles that can perform the events of type α (number of such particles per adsorption site) and m_α is the local multiplicity, i.e. the number of hops that each such particle can perform to a neighbouring position.

Similarly, the total adsorption rate and the total rate are described as:

$$R_a = \sum_{\alpha\in\{a\}} M_\alpha k_\alpha, \tag{3}$$

$$R = \sum_{\alpha\in\{e\}} M_\alpha k_\alpha, \tag{4}$$

where $\{a\}$ is the collection of distinct adsorption event types, $\{e\}$ is the collection of all distinct event types (diffusion and adsorption), and M_α is the multiplicity of the rate constant k_α (for the events of type α). Note that R_a, R and M_α are averaged quantities at three different levels (time-and-ensemble average per-site).

2.4. Probability of observing an event type

The total rate, R, is an instrumental quantity since it can be used directly to determine the *probability of observing event type* α *amongst all distinct diffusion and adsorption event types*:

$$\omega_\alpha^R = \frac{M_\alpha k_\alpha}{R} = \frac{M_\alpha k_\alpha}{\sum_{\alpha'\in\{e\}} M_{\alpha'} k_{\alpha'}}, \quad \alpha \in \{e\}. \tag{5}$$

Similarly, the total diffusion rate, R_d, can be used to determine the *probability of observing event type* α *amongst all distinct diffusion event types*:

$$\omega_\alpha^{R_d} = \frac{M_\alpha k_\alpha}{R_d} = \frac{M_\alpha k_\alpha}{\sum_{\alpha'\in\{d\}} M_{\alpha'} k_{\alpha'}}, \quad \alpha \in \{d\}. \tag{6}$$

Although both quantities are probabilities, their meaning is with respect to the collection of events considered in the denominator, thus justifying the superindex R or R_d, respectively. The *event probabilities* of equation (5) directly indicate which event types dominate the overall process, considering both adsorption and diffusion event types. The *event probabilities* of equation (6) indicate which diffusion event types dominate with respect to all distinct diffusion types.

2.5. Apparent activation energy

For an Arrhenius plot of the total rate [where $\log(R)$ is shown against inverse temperature, $\beta = 1/k_\mathrm{B}T$, where k_B is Boltzmann's constant and T is absolute temperature], the apparent activation energy is defined as:

$$E_\mathrm{app}^R = -\frac{\partial \log R}{\partial \beta}, \tag{7}$$

$$= -\frac{1}{R}\frac{\partial R}{\partial \beta}, \tag{8}$$

$$= -\frac{1}{\sum\limits_{\alpha\in\{e\}} M_\alpha k_\alpha}\frac{\partial\left(\sum_{\alpha\in\{e\}} M_\alpha k_\alpha\right)}{\partial \beta}, \tag{9}$$

where equation (4) has been used to write equation (9). Since the multiplicities for any given configuration of the system, M_α, depend on the actual values of the temperature-dependent rate constants, $k_\alpha = k_\alpha^0 \mathrm{e}^{-E_\alpha^k \beta}$, the multiplicities themselves are functions of temperature. Using $E_\alpha^M = -\frac{\partial \log M_\alpha}{\partial \beta}$, and applying the chain rule to $\sum_{\alpha\in\{e\}} M_\alpha k_\alpha$ in equation (9) easily leads to:

$$E_\mathrm{app}^R = \sum_{\alpha\in\{e\}} \epsilon_\alpha^R, \quad \text{with } \epsilon_\alpha^R = \omega_\alpha^R (E_\alpha^k + E_\alpha^M). \tag{10}$$

Here, ω_α^R is the probability of observing event type α considering all adsorption and diffusion event types, as given in equation (5). Note that, in general, an additional term, $E_\alpha^{k^0} = -\frac{\partial \log(k_\alpha^0)}{\partial \beta}$, should be added to $E_\alpha^k + E_\alpha^M$ in equation (10). However, $E_\alpha^{k^0}$ is zero in this study, since the prefactors k_α^0 are temperature-independent.

Similarly, recalling that the coverage is independent of temperature (since we use the same deposition flux at all temperatures), the apparent activation energy of the diffusivity, $E_\mathrm{app}^{D_\mathrm{T}} = -\frac{\partial \log D_\mathrm{T}}{\partial \beta}$, is easily determined by using equation (2) in (1). We obtain:

$$E_\mathrm{app}^{D_\mathrm{T}} = E^f + E_\mathrm{app}^{R_d}, \tag{11}$$

$$E_\mathrm{app}^{R_d} = \sum_{\alpha\in\{d\}} \omega_\alpha^{R_d} (E_\alpha^k + E_\alpha^M), \tag{12}$$

where $E^f = -\frac{\partial \log f_\mathrm{T}}{\partial \beta}$, $E_\alpha^k = -\frac{\partial \log k_\alpha}{\partial \beta}$ and $E_\alpha^M = -\frac{\partial \log M_\alpha}{\partial \beta}$ are the contributions from the correlation factor (f_T), the rate constant for the diffusion events of type α (k_α) and the multiplicity of that diffusion event type (M_α), respectively, and the weight $\omega_\alpha^{R_d}$ is the probability of observing diffusion type α amongst all distinct diffusion types (equation (6)). Since the contribution from the temperature dependence of the correlation factor is typically small ($E^\mathrm{f} \approx 0$), equation (11) shows that the temperature dependence of the diffusivity is essentially given by that of the total diffusion rate: $E_\mathrm{app}^{D_\mathrm{T}} = E^f + E_\mathrm{app}^{R_d} \approx E_\mathrm{app}^{R_d} = \sum_{\alpha\in\{d\}} \omega_\alpha^{R_d} (E_\alpha^k + E_\alpha^M)$. Again, this justifies the analysis of the total diffusion rate in this study, instead of the diffusivity itself.

According to equation (12), the contribution of event type α to the apparent activation energy of R_d is $\omega_\alpha^{R_d}(E_\alpha^k + E_\alpha^M)$. Simply speaking, $\omega_\alpha^{R_d}$ provides the relative importance of event type α as compared to all other diffusion events. Inside the bracket, the activation barrier for the event type, E_α^k, is modified by a configurational contribution, E_α^M, which describes how the multiplicity of that event type changes with temperature. Note that E^M_α is unbounded and can be positive, negative or zero, depending on the actual increase, decrease or constancy of M_α with respect to temperature. When the overall process is dominated by a single event type or *rate determining step*, say type λ, then $\omega^{R_d}_\lambda \approx 1$ and $\omega^{R_d}_\alpha \approx 0$ for all other event types, and we have: $E^{R_d}_{\mathrm{app}} = E^k_\lambda + E^M_\lambda$. In this manner, the apparent activation energy, $E^{R_d}_{\mathrm{app}}$, differs from the activation barrier of the rate determining step, E^k_λ, due to the change in the abundance of that particular event on the surface as a function of temperature, E^M_λ.

Note that the apparent activation energies of R and R_d have the same functional dependence (equations (10) and (12), respectively), differing only in the actual collection of considered events in the summation (both diffusion and adsorption events for R, and only the diffusion events for R_d), and the value of the weight, i.e. the probability with respect to all other considered events.

3. Results

For the actual simulations, we have used the software named ‘Morphokinetics’, written in object-oriented Java language and developed at the Donostia International Physics Centre. Morphokinetics is based on the standard, rejection-free, time-dependent implementation of the kinetic Monte Carlo (KMC) method with periodic boundary conditions [29, 33, 38, 54, 56]. See appendix A.4 for details. Morphokinetics enables simulating various surface-mediated processes, including anisotropic etching (removal of material from the substrate), heterogeneous catalysis (reactions on the substrate) and 2D monolayer growth (deposition of material on the substrate). The source code is freely available at the GitHub repository[6], with a free license GNU General Public License version 3 or any later version, which means that users have freedom to run, study, redistribute and improve the programme.

3.1. Island density

We first consider the island density, n_{isl}, defined for any given coverage as the ensemble average of the total number of islands divided by the total number of adsorption sites L_xL_y. Figure 4(a) shows that n_{isl} is higher for Cu/Ni(111) than for Ni/Cu(111) in all the temperature range, except for the highest temperatures. The plot corresponds to 10% coverage ($\theta = 0.10$), which is low enough to avoid potential coalescence of neighbour islands, while it is high enough to ensure the formation of stable islands. For both systems, the lower the temperature the larger the island density and, overall, the temperature dependence is similar. Nevertheless, for the same coverage and temperature, the particular value of the density is different.

This behaviour agrees well with traditional 2D nucleation theory [24, 57]:

$$n_{\mathrm{isl}} \propto \left(\frac{F}{D}\right)^{\frac{i}{i+2}}, \tag{13}$$

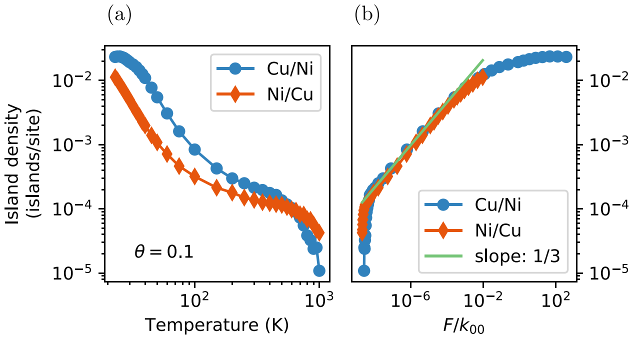

Figure 4. Average island density at 10% coverage for Cu/Ni(111) and Ni/Cu(111) from 23 K to 1000 K with complete-island and multi-atom diffusion events activated.

where F is the adsorption flux, $D = \frac{1}{2\delta}\frac{\langle \mathcal{R}^2\rangle}{t}$ is the diffusivity for a single monomer ($D = \frac{3}{4}k_{\mathrm{m}}l^2$ for the triangular lattice, with k_{m} the monomer diffusion rate and $l = 1$ the hop distance) and i is the critical island size (islands with size $> i$ are stable). Note that, under a constant deposition flux, one should use $D = \frac{3}{4}k_{\mathrm{m}}l^2$ for the triangular lattice instead of the traditional value $D = \frac{3}{2}k_{\mathrm{m}}l^2$, as explained in appendix A.3. In our case, the deposition flux F takes the same value and the critical island size i behaves practically the same in both systems (see next paragraph). However, $D \propto k_{\mathrm{m}}$ varies with the adatom type (Ni or Cu) and temperature. In fact, the monomer diffusion energy barrier is 52 meV for Cu/Ni(111) and 31 meV for Ni/Cu(111), which implies higher D for the Ni/Cu(111) system and, thus, lower island density. Therefore, the observed behaviour with temperature agrees with expectations, except at the highest temperatures, at which diffusion is not controlled anymore by the monomers and the critical island size deviates from one system to the other.

In fact, the plot of $\log(n_{\mathrm{isl}})$ vs $\log(F/k_{\mathrm{m}})$ in figure 4(b) shows that the two systems follow equation (13), with $i = 1$ and $x = \frac{i}{1+2} = \frac{1}{3}$ at medium temperatures (=medium F/k_{m}). This means that dimers are the smallest stable nuclei in this range. At low temperatures (high F/k_{m}), $n_{\mathrm{isl,Ni}}$ displays a tendency towards saturation, indicating that $i \approx 0$ for extremely low temperatures, i.e. monomers already form stable nuclei. This is due, literally, to the absence of diffusion and the dominant role of adsorption, as will be shown in section 3.3. Note that $n_{\mathrm{isl,Cu}}$ shows the same tendency at low temperatures. In turn, at high temperatures (low F/k_{m}), the slopes of $n_{\mathrm{isl,Ni}}$ and $n_{\mathrm{isl,Cu}}$ increase dramatically while slightly deviating from each other, indicating, as expected, that significantly more than two adatoms are required to stabilise a cluster and the actual diffusion events contributing to the stabilisation of the nuclei differ slightly from one system to the other.

3.2. Morphology

Not only the island density differs from one system to the other, their morphology deviates as well. This is shown in figures 5(a) and (e) for a collection of representative temperatures at $\theta = 0.10$. At the lowest temperatures islands are more dendritic in both systems, reflecting low diffusivity along island’s perimeters after monomer attachment. At

---

[6] https://github.com/dipc-cc/Morphokinetics.git.

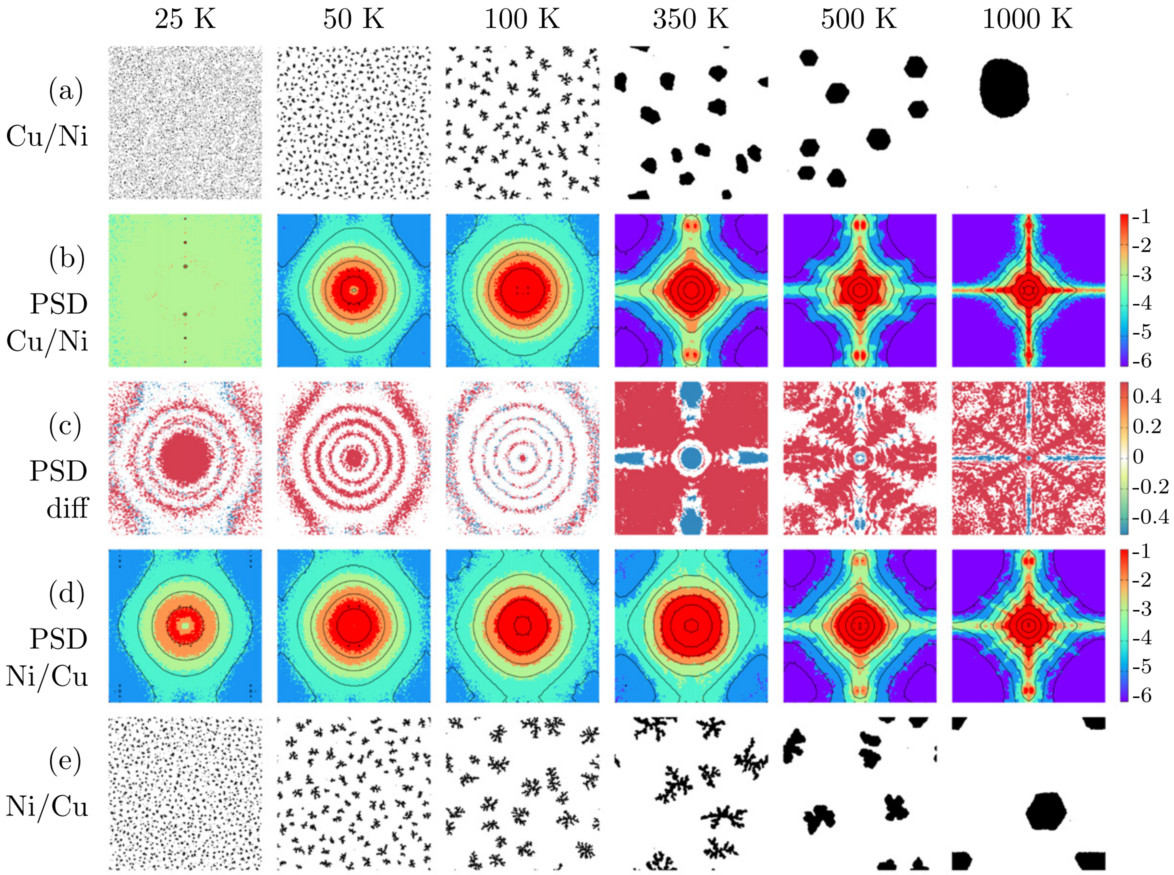

Figure 5. (a) and (e) Surface morphology for Cu/Ni(111) and Ni/Cu(111), respectively, at $\theta = 0.10$ and various temperatures (as indicated) with complete-island and multi-atom diffusion events activated. (b) and (d) PSD maps for Cu/Ni(111) (b) and Ni/Cu(111) (d). (c) PSD difference maps.

the highest temperatures, however, islands tend to be compact/hexagonal, reflecting high diffusivity at perimeters. In this case, adatoms move quickly along perimeters and are able to find the lowest energy sites (or thermodynamically stable positions).

The morphology of the islands reflects differences in the growth process. Simple visual inspection indicates that the island shapes are different, specially at 350 K, where Cu forms compact islands while Ni condensates into dendritic shapes. At the other temperatures, however, the distinction is less obvious and so a quantitative power spectral density (PSD) analysis is useful to show the actual variations [56, 58–60]. Here, an image of the surface is associated with a 2D map in which each location represents a harmonic frequency and the displayed value represents the squared sum of the real and imaginary amplitudes for that harmonic component (i.e., the power for that frequency). Lower frequencies are correlated with large structures, such as the overall shape of the islands, while larger frequencies are related to small features, such as the structure of the perimeter. In this manner, the PSD analysis enables comparing different/similar surfaces with stochastic variations. In fact, two PSD maps can be considered equivalent when their point-to-point difference produces noise (= stochastic fluctuations) around the 0 value all over the resulting difference map. On the contrary, when two PSDs differ structurally, their difference map displays distinctive patterns, clearly deviating from random fluctuations around the 0 value. By using the images from 10 equivalent simulations with different random numbers, the corresponding average PSD maps are shown in figure 5(b) for Cu/Ni(111) and figure 5(d) for Ni/Cu(111). In addition, point-by-point PSD difference maps are shown in figure 5(c).

At 25 K, where visual inspection is difficult, the PSD difference map displays several circular patterns, clearly deviating from random fluctuations around the 0 value (noise) and, thus, concluding that the two surfaces differ structurally. Note that perfect noise on the PSD difference map is indicated by random blue/red/white values associated with positive/negative/zero fluctuations between the two maps. At 50 K, the PSD difference map is essentially the same as for 25 K, thus revealing structural differences. At 100 K, where both PSD maps are the most similar, the difference map still shows circles. At the already considered temperature of 350 K, the Cu/Ni(111) map displays considerably higher values, except at the central and cross-like regions, where it is lower. At 500 K, the PSD difference map still reveals a strong structural mismatch. Here, the Cu/Ni(111) islands are almost hexagonal while the Ni/Cu(111) islands still remain amorphous. At the highest considered temperature (1000 K), both islands are compact. However, the shape for Cu/Ni(111) resembles

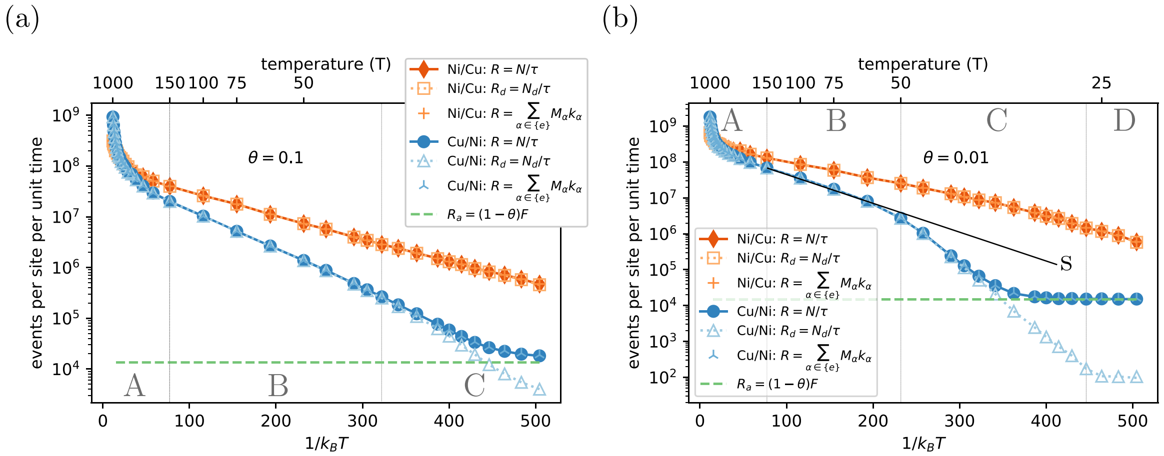

Figure 6. Average total rates per site for diffusion (R_d), adsorption (R_a) and all events ($R = R_d + R_a$) for Cu/Ni(111) and Ni/Cu(111), as indicated, (a) at 10% coverage and (b) at 1% coverage.

a circle while that for Ni/Cu(111) approaches a hexagon; the PSD map for Cu/Ni(111) is mostly higher than that for Ni/Cu(111), with significantly lower values at the centre and at four elongated horizontal/vertical regions. Overall, comparing the two systems at the same temperature and coverage, we conclude that they display different island densities and morphologies.

3.3. *Total rate, total diffusion rate and total adsorption rate*

In addition to the differences in the island density and morphology, also the average total rate per site, $R = N/\tau$ (equation (A.25) of the appendix), differs between the two systems. This is shown in the Arrhenius plot in figure 6(a) for $\theta = 0.10$ and $T = 23$–1000 K, while the case for $\theta = 0.01$ is shown in figure 6(b) and many other coverage values are considered in figures C1 and C2 of the appendix. These figures also display the average total rate per site determined using equation (A.28) of the appendix (=equation (2)), $R = \sum_{\alpha\in\{e\}} M_\alpha k_\alpha$, demonstrating that both equations (A.25) and (A.28) provide equivalent descriptions of the same quantity. In addition, the figures also show the average total diffusion rate per site, $R_d = N_d/\tau$ $(= \sum_{\alpha\in\{d\}} M_\alpha k_\alpha)$ for the two systems and the average total adsorption rate per site, $R_a = N_a/\tau$ $(= \sum_{\alpha\in\{a\}} M_\alpha k_\alpha)$, which is identical for both systems and independent of temperature, only depending on coverage: $R_a = \sum_{\alpha\in\{a\}} M_\alpha k_\alpha = M_a k_a = (1-\theta)F$.

Regarding figure 6(a), the total rate is much higher in the Ni/Cu(111) system, specially at low temperatures (e.g. region C). Since adsorption is identical in both systems and remains quite low, the difference in their total rate is primarily due to the total diffusion rate, which is higher for Ni/Cu(111). Nevertheless, in the Cu/Ni(111) system adsorption plays an important role at the lowest temperatures (region C), where it provides the largest contribution to the total rate, significantly over the total diffusion rate. In fact, the adsorption rate (1.5×10^4 Hz) is higher than the monomer diffusion rate at 25 K (3.3×10^2 Hz for a diffusion barrier of 52 meV). This behaviour is noticeable until about 32 K (the frontier between regions B and C), above which the total rate is essentially dominated by the total diffusion rate, as for the Ni/Cu(111) over the whole considered range of temperature.

At lower coverage, more complex behaviour is observed at low temperatures, as shown in regions C and D of figure 6(b), especially in the case of R_d for Cu/Ni(111). As shown in section 3.4 below, the diffusivity in this case (R_d for Cu/Ni(111)) is dominated by non-concerted dimer diffusion in regions C and D and it is ruled by monomer diffusion in region B. In region A, monomer diffusion is complemented by perimeter diffusion and both concerted and non-concerted dimer diffusion, in addition to other secondary events. Although non-concerted dimer diffusion dominates in both regions C and D, it has not yet really been activated in region D. The behaviour for the total rate R of Cu/Ni(111) is similar to that of R_d, but R remains higher than R_d at low temperatures due to the larger value of the total adsorption rate (R_a). Finally, the trend for Ni/Cu(111) in figure 6(b) is similar, but displaced towards lower temperatures.

3.4. *Activation energy*

For the Arrhenius plot in figure 6(a), the slope of R vs β is the apparent activation energy, E^R_{app}, which is shown in figure 7(a) for Ni/Cu(111) and figure 7(b) for Cu/Ni(111). While these plots correspond to $\theta = 0.10$ and $T = 23$–1000 K, similar results for additional coverage values are shown in figures C5 and C6 of the appendix. In each plot, we show two temperature regions: (I) $1000 \geqslant T > 150$ K, and (II) $150 \geqslant T \geqslant 23$ K, with the low temperature region displayed in a magnified view. In addition, each region shows two alternative expressions for the apparent activation energy, namely, $E^R_{\text{app}} = -\frac{\partial \log R}{\partial \beta}$ with $R = N/\tau$ (equations (7) and (A.25) of the appendix, respectively) and $E^{R,*}_{\text{app}} = \sum_{\alpha\in\{e\}} \epsilon^R_\alpha$ with $\epsilon^R_\alpha = \omega^R_\alpha(E^k_\alpha + E^M_\alpha)$ (equation (10)). The former (E^R_{app} in the plots) is obtained numerically by using finite central differences of $\log R$ and β. The latter ($\sum_{\alpha\in\{e\}} \epsilon^R_\alpha$ in the plots) is obtained from the rate of every event type, k_α, and the corresponding multiplicity, M_α, in order to determine the probability of every event type, ω^R_α (equation (5)), as well as by summing the energy barrier, E^k_α, and the configurational contribution, $E^M_\alpha = -\frac{\partial \log M_\alpha}{\partial \beta}$, calculated by finite

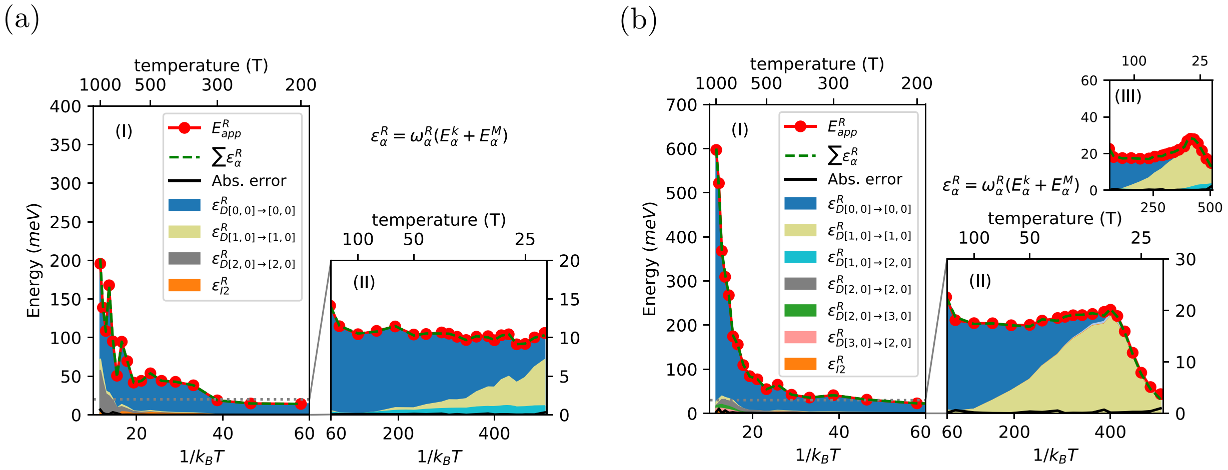

Figure 7. Temperature dependence of the apparent activation energy of the average total rate per site (E^R_{app}) at $\theta = 0.10$ for (a) Ni/Cu(111) and (b) Cu/Ni(111). E^R_{app} is described well by $\sum_{\alpha\in\{e\}}\epsilon^R_\alpha$, where $\epsilon^R_\alpha = \omega^R_\alpha(E^k_\alpha + E^M_\alpha)$. The absolute error $|E^R_{\text{app}} - \sum_{\alpha\in\{e\}}\epsilon^R_\alpha|$ is also plotted. The inset labelled 'III' in frame (b) displays the apparent activation energy of the total diffusion rate per site, $E^{R_d}_{\text{app}}$.

differences as well. In addition, each plot shows the absolute error between the two measures, $|E^R_{\text{app}} - \sum_{\alpha\in\{e\}}\epsilon^R_\alpha|$, which remains smaller than 6.65 meV for Ni/Cu(111) and 3.12 meV for Cu/Ni(111), with a mean value of 0.49 meV for Ni/Cu(111) and 0.51 meV for Cu/Ni(111). The maximum error is typically due to the finite difference estimate of the slope (not the multiplicity based formula) and it usually occurs at the highest/lowest temperature or when $\log R$ fluctuates with respect to the previous temperature. Thus, figures 7(a) and (b) show that equation (10) accurately explains the values observed for the apparent activation energy.

Next, we analyse the different contributions to the apparent activation energy. Before that, however, it is useful to note that, for Ni/Cu(111) in figure 7(a), the apparent activation energy of the total rate, E^R_{app}, is also the apparent activation energy of the total diffusion rate, $E^{R_d}_{\text{app}} = E^R_{\text{app}}$, since $R = R_d$ in this system (see figure 6(a)). In turn, based on equation (12), the apparent activation energy of the diffusivity is: $E^{D_{\text{T}}}_{\text{app}} \approx E^{R_d}_{\text{app}} = E^R_{\text{app}}$, since the contribution from the correlation factor, $E^{f_{\text{T}}} = -\frac{\partial \log f_{\text{T}}}{\partial\beta}$, is very small [33].

Since the apparent activation energy is constant ($\approx$ 10 meV) in region II of figure 7(a) for Ni/Cu(111), traditionally one would be tempted to conclude that there is a single rate-controlling event in this temperature range. However, 10 meV does not correspond to any of the energy barriers included in the system. In fact, the multiplicity analysis based on equation (10), $E^R_{\text{app}} = \sum_{\alpha\in\{e\}}\epsilon^R_\alpha = \sum_{\alpha\in\{e\}}\omega^R_\alpha(E^k_\alpha + E^M_\alpha)$, shows that there are three main contributing events in this region, namely, monomer diffusion ($D[0,0] \to [0,0]$, with $E^k_{D[0,0]\to[0,0]} = 31$ meV), non-concerted dimer diffusion ($D[1,\ 0] \to [1,\ 0]$, with $E^k_{D[1,0]\to[1,0]} = 16$ meV), and concerted dimer diffusion (I2, with $E^k_{\text{I2}} = 21$ meV). The major contribution shifts from (non-concerted + concerted) dimer diffusion at the lowest temperatures (where the chance to form dimers is high) towards monomer diffusion at the highest temperatures in this range (where recently adsorbed monomers have a larger chance to reach an island than to form a dimer). Note that the shift is mostly due to the change in the event probabilities, ω^R_α, with temperature for those three particular event types, as shown in figure 8(a). In addition, the configurational contributions to the apparent energy for the three event types, $E^M_{D[0,0]\to[0,0]}$, $E^M_{D[1,0]\to[1,0]}$ and E^M_{I2}, are negative in this case, thus leading to a value of the apparent activation energy ($\approx$ 10 meV) that is significantly smaller than any of the three energy barriers (31, 16 and 21 meV).

For the lowest temperatures ($T < 60$ K), figure 8(a) shows that several additional event types have appreciable roles, with probabilities larger than 0.1% and up to about 3%. This includes adsorption (no energy barrier), monomer attachment to the islands ($D[0,0] \to$ [1, 0] and $D[0,0] \to$ [2, 0], with energy barriers of 28 and 15 meV, respectively) and perimeter adatom stabilisation ($D[1,\ 0] \to$ [2, 0], 14 meV; $D[1,\ 0] \to$ [2, 2], 0 meV; and $D[1,\ 0] \to$ [3, 0], 1 meV). Furthermore, concerted dimer diffusion (I2, with $E^k_{\text{I2}} = 21$ meV) has an appreciable role over the complete temperature range, with an event probability of 8–10% up to about 50 K, and remaining active at higher temperatures ($\geqslant$1%). Finally, at the highest temperatures, edge diffusion ($D[2,0] \to [2,0]$, with $E^k_{D[2,0]\to[2,0]} = 364$ meV), trimer diffusion ($I3$, with $E^k_{I3} = 148$ meV) and a few other processes become relevant, with event probabilities larger than 0.1%.

Here, the energy barrier for non-concerted dimer diffusion (16 meV) is smaller than that for concerted dimer diffusion (21 meV) and, thus, non-concerted diffusion has a larger rate, especially at low temperatures (e.g. $k_{D\ [1,0]\to[1,0]} = 3.1 \times 10^9$ Hz and $k_{\text{I2}} = 2.5 \times 10^8$ Hz at 23 K). On the other hand, the multiplicities of the two event types are similar, with $M_{D[1,0]\to[1,0]} = 4n_2$ (where n_2 is the density of dimers and both atoms may hop in two directions while remaining attached to the other, thus leading to a multiplicity of $2 \times 2 = 4$ per dimer) while $M_{\text{I2}} = 6n_2$ (since there are six hop directions in the triangular lattice). Thus, comparing the total rates per site for both

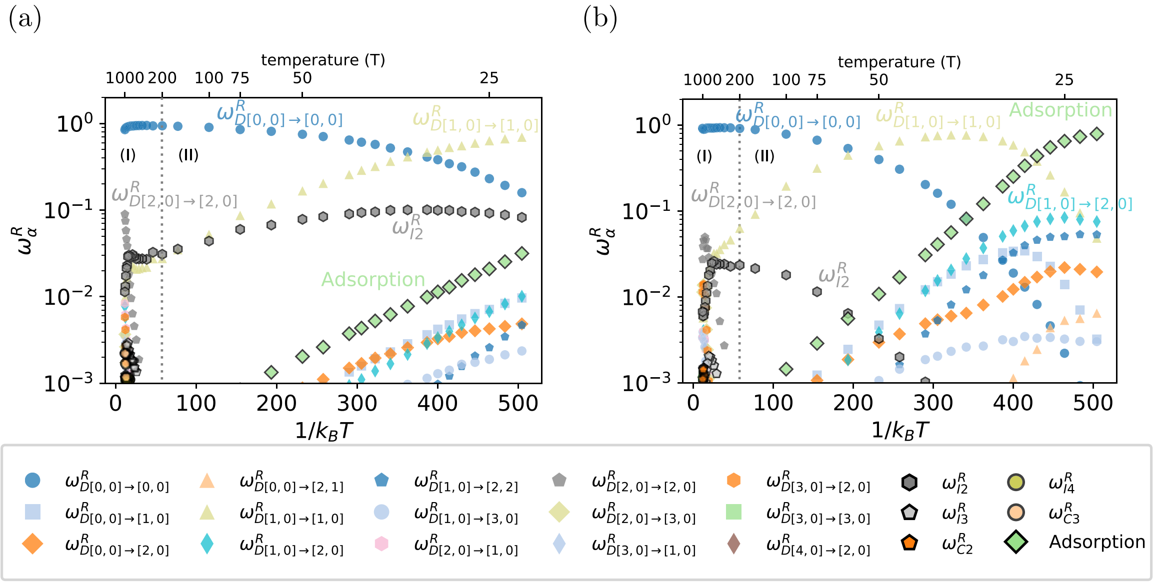

Figure 8. Temperature dependence of the event probabilities, w^R_α, at $\theta = 0.10$ for (a) Ni/Cu(111) and (b) Cu/Ni(111). Only those events whose probability is higher than 10^{-3} are shown.

events, $4n_2k_{D[1,0]\to[1,0]}$ and $6n_2k_{\mathrm{I2}}$, non-concerted dimer diffusion occurs more often at low temperatures. However, at high temperatures the two rates become very similar and concerted dimer diffusion occurs more frequently due to the slightly larger multiplicity. See figure C4 in the appendix for further proof. Based on this example, we believe that there may be systems where concerted dimer diffusion dominates over non-concerted diffusion in a wide range of temperature.

For Cu/Ni(111) in figure 7(b), the situation is very similar, except for the fact that E^R_{app} approaches zero at the low temperature end. In this region, the total rate is dominated by adsorption, $R = R_a = M_a k_a$ (see figure 6(a)), with both the adsorption rate, $k_a = F$, and the multiplicity, $M_a = 1 - \theta$, being temperature independent. Thus, $\epsilon^R_a = \omega^R_a(E^k_a + E^M_a) = 0$, because $E^k_a = E^M_a = 0$ even though $w^R_a \approx 1$ (see figure 8(b)).

The inset in figure 7(b) for $\theta = 0.1$ displays the apparent activation energy of the total diffusion rate per site, $E^{R_d}_{\mathrm{app}}$, characterised by a weak maximum in the range 23–50 K, which is clearly assigned to the temperature dependence of $\epsilon^R_{D[1,0]\to[1,0]}$ (non-concerted dimer diffusion). Note that a similar maximum is observed in the inset of figure C5 for $\theta = 0.01$ in the appendix and it is also assigned to $\epsilon^R_{D[1,0]\to[1,0]}$. For such low temperatures, the quickly-diffusing dimers (through non-concerted diffusion) collide against the slowly-diffusing monomers (which essentially act as stationary obstacles). This generates both triangular (immobile) and chain-like (mobile) trimers, which are eventually compacted into the triangular (immobile) shape via perimeter adatom stabilisation ($D[1, 0] \to [2, 0]$ and $D[1, 0] \to [2, 2]$). The maxima in $\epsilon^R_{D[1,0]\to[1,0]}$ in the insets of figure 7(b) for $\theta = 0.1$ and figure C5 for $\theta = 0.01$ correlate with the peaks in the probability of generating dimers, $\omega^R_{D[0,0]\to[1,0]}$, as shown in figure 8(b) for $\theta = 0.1$ and figure C7 for $\theta = 0.01$, respectively. Thus, as the temperature is increased, a larger fraction of the monomers start diffusing and, as a result, there are less obstacles and a lower probability to form dimers. Consequently, the dominance by dimer diffusion gives away to the dominance by monomer diffusion.

According to figure 8(b), the biggest difference with respect to Ni/Cu(111) at low temperature is the strong dominance by adsorption (no energy barrier), monomer attachment to the islands ($D[0,0] \to [1, 0]$ and $D[0,0] \to [2, 0]$, with energy barriers of 35 and 31 meV, respectively) and stabilisation of recently-attached monomers ($D[1, 0] \to [2, 0]$, 26 meV; $D[1, 0] \to [2, 2]$, 10 meV; and $D[1, 0] \to [3, 0]$, 10 meV). Note that, in the Cu/Ni(111) system, the role of concerted dimer diffusion (I2) is less significant, achieving an event probability of between 0.1 and 2.8% at high temperatures. Similarly, at the highest considered temperatures, edge diffusion ($D[2, 0] \to [2, 0]$, with $E^k_{[2,0]\to[2,0]} = 268$ meV) becomes appreciable.

Further plots for the event probabilities as a function of temperature are shown for representative coverages in figures C7 and C8 of the appendix, for Cu/Ni(111) and for Ni/Cu(111), respectively. The trend at any coverage is much equivalent to the picture just presented. In general, the Cu/Ni(111) system is dominated by monomer diffusion ($D[0,0] \to [0,0]$) at high temperatures, non-concerted dimer diffusion ($D[1,0] \to [1,0]$) at intermediate temperatures, and adsorption at low temperatures. At this end (low temperature), monomer attachment to the islands ($D[0,0] \to [1, 0]$, $D[0,0] \to [2, 0]$ and $D[0,0] \to [3, 0]$) and stabilisation of recently-attached monomers ($D[1, 0] \to [2, 0]$, $D[1, 0] \to [2, 2]$ and $D[1, 0] \to [3, 0]$) are also relevant, becoming more important the lower the temperature and the higher the coverage, each one on a different scale. The same trend is valid for the Ni/Cu(111) system, although the importance of adsorption, monomer attachment and recently-attached-monomer stabilisation at low temperatures is less significant. In addition, concerted dimer diffusion has an appreciable role in this system at all coverages and over the whole range of temperature. For completeness, the event probabilities for the most relevant events are also shown as three-dimensional plots against coverage and inverse temperature in figures C9 and C10 of the appendix, for for Cu/Ni(111) and for Ni/Cu(111), respectively.

4. Conclusions

We develop a scheme to perform kinetic Monte Carlo simulations of sub-monolayer growth on the fcc(111) surface and use it to study aggregation on two hetero-epitaxial systems, namely, Cu on Ni(111) and Ni on Cu(111). By including a large variety of single-atom, multi-atom and complete-island diffusion events, the two systems are compared in terms of their coverage- and temperature-dependent morphology, island density and tracer diffusivity (or overall diffusion constant). In particular, the diffusivity is shown to be proportional to the total diffusion rate, which is described as a simple sum over all different diffusion rate constants, one for every diffusion event type, each multiplied by the corresponding multiplicity, i.e. the abundance of that event type on the surface. As an advantage of the multiplicity approach, we conclude that, at low temperatures, the diffusivity is dominated by dimer diffusion, which is split between non-concerted and concerted dimer diffusion. At medium temperatures, it is controlled by monomer diffusion and, at high temperatures, it is due to a mixture of monomer diffusion, perimeter diffusion and concerted dimer/trimer diffusion. Thus, this work shows the importance of some concerted diffusion events in 2D sub-monolayer epitaxial growth. The substantial role of concerted diffusion in one of the two analysed systems suggests that concerted motion in general may be dominant in other systems, including the relatively unexplored area of on-surface synthesis.

More importantly, the use of the multiplicities enables formulating the apparent activation energy as a weighted average, where the weights are identified as the probabilities of the different events and the actual energy contribution for every event contains both the traditional energy barrier and an additional unbounded configurational term, directly related to the temperature dependence of its multiplicity. Since the leading event in the weighted average may easily change with the growth conditions and the configurational terms may vary widely, we show that a constant value of the apparent activation energy can be obtained even if control shifts from one elementary reaction to another. This means that the traditional assignment of a constant apparent activation energy to an underlying rate determining step is not the only possibility and, thus, it is not necessarily valid during submonolayer growth.

This study demonstrates that the multiplicity analysis can be applied for systems with hundreds of distinct events, showing that eventually a few of them dominate the growth process. In the future, the addition of self-learning KMC (SLKMC) [52, 54] techniques should enable finding and executing new diffusion events, for any type of single-atom and multi-atom event. The present work opens the door to include a multiplicity analysis into existing SLKMC methods.

Acknowledgments

We acknowledge support by the project US National Science Foundation grant DMR-1710306 (SRA and TSR) and by the Basque Departamento de Educacion, UPV/EHU (Grant No. IT-756-13), and the 2015/01 contract by the DIPC. The KMC calculations were performed on the ATLAS supercomputer in the DIPC. We would like to acknowledge STOKES advanced computing centre at the University of Central Florida for resources to calculate barriers of processes. We are thankful to Dr N Ferrando from Universitat Politècnica de València, for the main development of the PSD tool as well as an initial implementation of the 'Morphokinetics' KMC code.

Appendix A. Theoretical background

The following presentation resembles closely that given in reference [61] for the more general case of heterogeneous catalysis. In that case, the adsorption and desorption rate constants are both pressure- and temperature-dependent, while the adsorbates may diffuse across the surface with neighbourhood-dependent rate constants and recombination reactions may take place between neighbouring adsorbates. Below, we focus on systems where desorption and recombination are essentially irrelevant (very low rates).

A.1. Total diffusion rate, total adsorption rate and total rate

To study the adsorption and diffusion of adatoms of Ni on Cu(111) and Cu on Ni(111), we consider a two-dimensional lattice of adsorption sites under the same deposition flux F at any temperature [33–37]. For both systems, the substrate is treated as a two-dimensional triangular lattice, where atoms from the surrounding environment are deposited randomly (on the empty sites) while previously adsorbed adatoms are able to diffusive according to the particular diffusion event types considered in section 2.2 for single atoms, multiple atoms and complete islands.

The use of a constant deposition flux corresponds to a temperature-independent adsorption rate constant, $k_a = F$. As usual, we assume that the occupation state of the neighbourhood of an empty site (where adsorption may occur) does not affect the value of the adsorption rate constant [33–37]. Also as usual, the rate constant for a diffusion event of type α, k_α, is both neighbourhood- and temperature-dependent, and given by transition state theory (TST):

$$k_\alpha = k_0 \mathrm{e}^{-E^k_\alpha / k_\mathrm{B} T}. \tag{A.1}$$

Here, k_B is the Boltzmann constant, T is the temperature, E^k_α is the neighbourhood-dependent energy barrier for the diffusion events of type α and k_0 is the attempt frequency, which depends weakly on temperature and is usually assigned the value of 10^{13} Hz.

Considering the diffusion of all adatoms collectively, the instantaneous total diffusion rate is defined as:

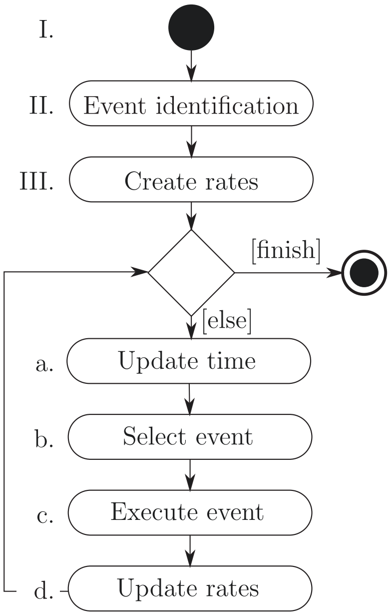

Figure A1. Unified modelling language (UML) activity diagram of a generic KMC algorithm.

$$\hat{r}_d = \sum_{\alpha\in\{d\}} \hat{m}_\alpha k_\alpha. \tag{A.2}$$

Here, the hat symbol (ˆ) is used over any time-dependent variable (e.g. X) to denote the instantaneous value of that variable at time t: $\hat{X} = X(t)$. In this manner, $\hat{m}_\alpha$ is the instantaneous value of the multiplicity for event type α, i.e. the number of times the event type α can be performed at the particular configuration of the surface observed at time t. Finally, k_α is the diffusion rate constant for event type α, and $\{d\}$ is the collection of all distinct diffusion events. Thus, one obtains the total hop rate by summing over all different hop rates, each multiplied by the corresponding abundance on the surface (multiplicity) at time t.

Similarly, the instantaneous total adsorption rate is:

$$\begin{aligned} \hat{r}_a &= \sum_{\alpha\in\{a\}} \hat{m}_\alpha k_\alpha, && \text{(A.3)}\\ &= \hat{m}_a k_a, && \text{(A.4)}\\ &= (1-\hat{\theta})L_xL_yk_a = L_xL_y\mathrm{e}^{-k_at}k_a, && \text{(A.5)} \end{aligned}$$

where $\{a\}$ is the collection of distinct adsorption events, and $\hat{m}_\alpha$ (k_α) is the instantaneous multiplicity (adsorption rate constant) for event type α. Since we consider only one adsorption event type ($k_a = F$, independently of the neighbourhood), the summation in equation (A.3) is reduced to a single term, as indicated in equation (A.4). Here, $\hat{m}_a$ is the instantaneous adsorption multiplicity, i.e. the total number of empty sites at time t. Note that $\hat{m}_a = (1-\hat{\theta})L_xL_y$ in equation (A.5), where $\hat{\theta} = \hat{n}_a/L_xL_y$ designates the coverage, with $\hat{n}_a$ being the total number of adsorbed atoms at time t (i.e. the total number of adsorption events until time t) and L_xL_y the total number of adsorption sites (before adsorption of any atom). Due to the constant deposition flux, the coverage increases with time according to the equation: $\frac{\mathrm{d}\hat{\theta}}{\mathrm{d}t} = k_a(1-\hat{\theta})$, which is directly integrated to give: $\hat{\theta} = 1 - \mathrm{e}^{-k_at}$. Thus, $\hat{m}_a = L_xL_y\mathrm{e}^{-k_at}$ independently of the temperature.

Finally, since both diffusion and adsorption events may occur, we consider the instantaneous total rate:

$$\begin{aligned} \hat{r} &= \sum_{\alpha\in\{e\}} \hat{m}_\alpha k_\alpha, && \text{(A.6)}\\ &= \sum_{\alpha\in\{d\}} \hat{m}_\alpha k_\alpha + \sum_{\alpha\in\{a\}} \hat{m}_\alpha k_\alpha, && \text{(A.7)}\\ &= \sum_{\alpha\in\{d\}} \hat{m}_\alpha k_\alpha + \hat{m}_a k_a, && \text{(A.8)}\\ &= \hat{r}_d + \hat{r}_a, && \text{(A.9)} \end{aligned}$$

where $\{e\}$ is the collection of all distinct event types (diffusion and adsorption). In addition, the total number of performed events is: $\hat{n} = \hat{n}_d + \hat{n}_a$, where $\hat{n}_d$ is the total number of performed hops and $\hat{n}_a$ is the total number of executed adsorptions (as already defined above).

Dividing by the total number of sites, L_xL_y, we define the *instantaneous total rates per site*:

$$\hat{R}_d = \hat{r}_d/L_xL_y, \tag{A.10}$$

$$\hat{R}_a = \hat{r}_a/L_xL_y, \tag{A.11}$$

$$\hat{R} = \hat{r}/L_xL_y, \tag{A.12}$$

the *instantaneous total number of performed events per site*:

$$\hat{N}_d = \hat{n}_d/L_xL_y, \tag{A.13}$$

$$\hat{N}_a = \hat{n}_a/L_xL_y, \tag{A.14}$$

$$\hat{N} = \hat{n}/L_xL_y, \tag{A.15}$$

and the *instantaneous multiplicity per site*:

$$\hat{M}_\alpha = \hat{m}_\alpha/L_xL_y. \tag{A.16}$$

For simplicity, both $\hat{m}_\alpha$ and $\hat{M}_\alpha$ are referred to as the *instantaneous multiplicity*, although $\hat{M}_\alpha$ should be understood as a relative abundance or concentration. Similarly, $\hat{R}_d$, $\hat{R}_a$ and $\hat{R}$ are referred to as the *instantaneous total rates*, thus obviating their per-site character.

The instantaneous total diffusion rate, $\hat{R}_d$, is important, since the diffusion constant (or diffusivity) is proportional to the time-and-ensemble average of $\hat{R}_d$, as shown below (equation (A.32)). Similarly, the instantaneous total rate, $\hat{r}$, is also important, since the inverse of $\hat{r}$ provides a natural measure of the time increment between two events: $\Delta t = -\log(u)/\hat{r}$, where $u \in (0,1]$ is a uniform random number. By definition, $\hat{r}$ is equal to the number of performed events per unit time, $\hat{r} = \frac{\mathrm{d}\hat{n}}{\mathrm{d}t}$, and thus, $\hat{r} = \frac{1}{\Delta t}$, since exactly one event occurs per time step. With a mean value of 1, the positive factor $-\log(u)$ enforces the correct Poisson distribution for the time steps.

Now, for a time-dependent variable, $\hat{X}$, we consider the usual definition for its time average: $\overline{\hat{X}} = \frac{\int \hat{X}\,\mathrm{d}t}{\int \mathrm{d}t} = \frac{\Sigma_k \hat{X}_k \Delta t_k}{\Sigma_k \Delta t_k}$.

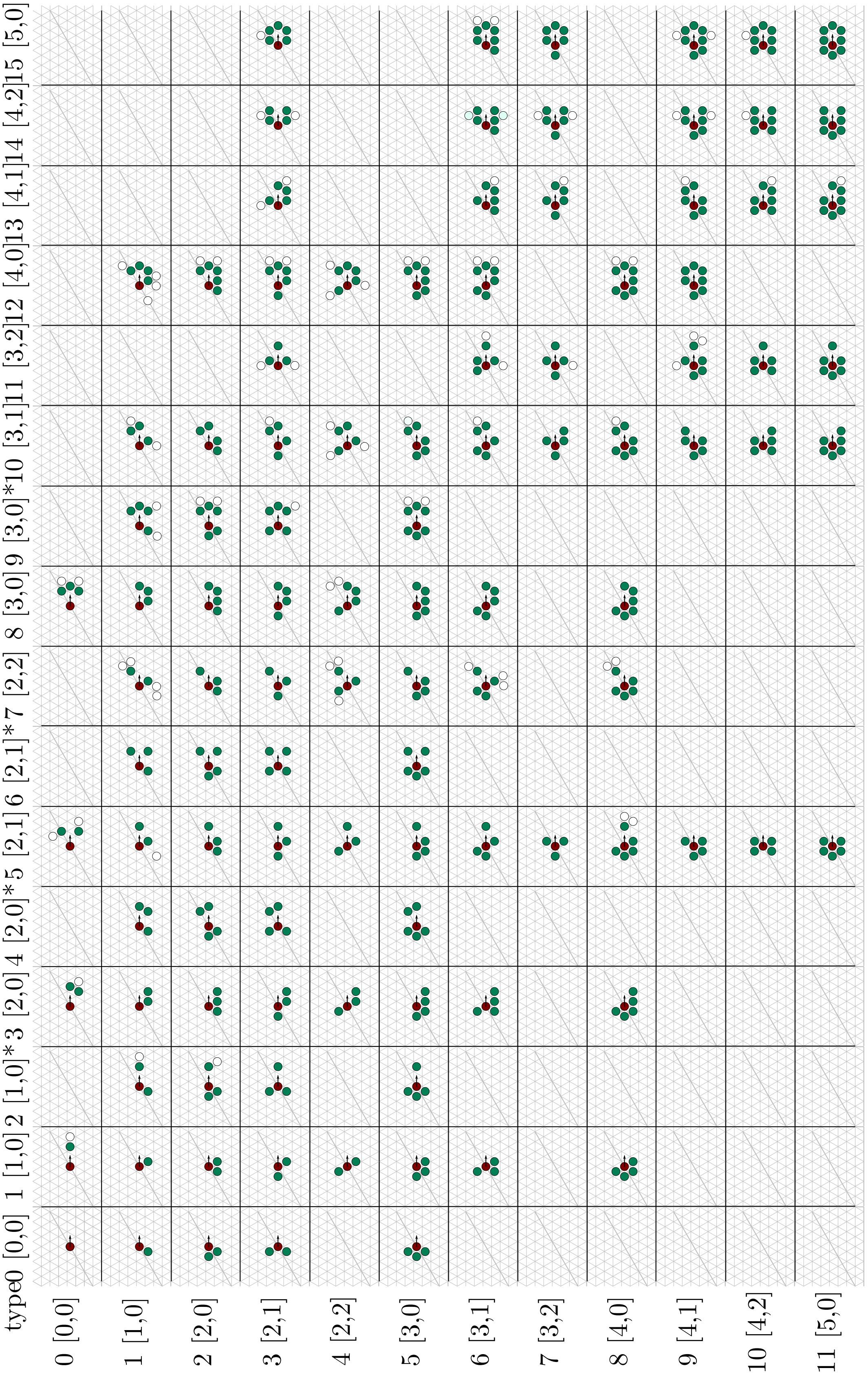

Figure B1. Complete table for all single-atom diffusion events considered in this study. The red adatom is moved one position to the right. The green adatoms are nearest neighbours of the origin/destination sites. White adatoms have been used to stabilise the structures in EAM + drag. * denotes detachment, where the destination site has no neighbours in common with the origin site. The table contains 107 single atom event types. Taking into account concerted island diffusion (7 types, figure 3(a)), multi-atom diffusion (4 types, figure 3(b)) and the adsorption event (1 unique event type), the KMC simulations use a total of 119 different event types.

Table B1. Microscopic diffusion activation energy barriers (in eV) for Cu/Ni system.

Type	Single atom diffusion events															
[class, subclass]	0 [0,0]	1 [1,0]	2 [1,0]*	3 [2,0]	4 [2,0]*	5 [2,1]	6 [2,1]*	7 [2,2]	8 [3,0]	9 [3,0]*	10 [3,1]	11 [3,2]	12 [4,0]	13 [4,1]	14 [4,2]	15 [5,0]
0 [0,0]	0.052	0.044	×	0.029	×	0.005	×	×	0.0024	×	×	×	×	×	×	×
1 [1,0]	0.428	0.038	0.317	0.026	0.258	0.033	0.183	0.0027	0.01	0.184	0.0012	×	0.00086	×	×	×
2 [2,0]	0.736	0.360	0.625	0.268	0.433	0.261	0.383	0.167	0.22	0.396	0.164	×	0.144	×	×	×
3 [2,1]	0.750	0.397	0.565	0.308	0.206	0.293	0.167	0.197	0.258	0.179	0.185	0.651	0.176	0.503	0.439	0.430
4 [2,2]	×	0.403	×	0.198	×	0.189	×	0.373	0.413	×	0.328	×	0.292	×	×	×
5 [3,0]	1.010	0.663	0.828	0.546	0.483	0.539	0.413	0.390	0.473	0.400	0.369	×	0.357	×	×	×
6 [3,1]	×	0.697	×	0.502	×	0.479	×	0.360	0.386	×	0.188	0.905	0.184	0.804	0.683	0.615
7 [3,2]	×	×	×	×	×	0.899	×	×	×	×	0.748	1.01	×	0.841	0.687	0.726
8 [4,0]	×	0.947	×	0.748	×	0.957	×	0.851	0.627	×	0.448	×	0.423	×	×	×
9 [4,1]	×	×	×	×	×	1.010	×	×	×	×	0.895	1.107	0.763	0.855	0.813	0.763
10 [4,2]	×	×	×	×	×	1.020	×	×	×	×	0.815	0.964	×	0.807	0.733	0.729
11 [5,0]	×	×	×	×	×	1.144	×	×	×	1.010	1.152	1.008	×	0.904	0.908	0.908

Concerted island diffusion			
Atoms in the island	Type	Energy (eV)	Name
2	I2	0.062	Dimer
3	I3	0.161	Trimer
4	I4	0.182	Tetramer
5	I5	0.222	Pentamer
6	I6	0.201	Hexamer
7	I7	0.403	Heptamer
8	I8	0.372	Octamer

Concerted two-atom diffusion	
Multi-atom type	Energy (eV)
C1	0.481
C2	0.437
C3	0.397
C4	0.228

Making the observation that $\hat{r}_d$ is equal to the number of performed diffusion events per unit time, $\hat{r}_d = \frac{\mathrm{d}\hat{n}_d}{\mathrm{d}t}$ (similar to $\hat{r} = \frac{\mathrm{d}\hat{n}}{\mathrm{d}t}$), the time average of $\hat{r}_d$ for any desired period (e.g. from 0 to t) can be written exactly as the total number of performed diffusion events, $\hat{n}_d$, divided by the elapsed time, t (and similarly for $\hat{r}_a$ and $\hat{r}$):

$$\overline{\hat{r}_d} = \frac{\int \hat{r}_d \,\mathrm{d}t}{\int \mathrm{d}t} = \frac{\int \frac{\mathrm{d}\hat{n}_d}{\mathrm{d}t}\,\mathrm{d}t}{t} = \frac{\int \mathrm{d}\hat{n}_d}{t} = \frac{\hat{n}_d}{t}, \tag{A.17}$$

$$\overline{\hat{r}_a} = \frac{\hat{n}_a}{t}, \tag{A.18}$$

$$\overline{\hat{r}} = \frac{\hat{n}}{t}. \tag{A.19}$$

Similarly, one obtains the following exact expressions:

$$\overline{\hat{R}_d} = \frac{\hat{N}_d}{t}, \tag{A.20}$$

$$\overline{\hat{R}_a} = \frac{\hat{N}_a}{t}, \tag{A.21}$$

$$\overline{\hat{R}} = \frac{\hat{N}}{t}. \tag{A.22}$$

In addition, for a time-dependent variable, $\hat{X}$, we consider its ensemble average, $\langle\hat{X}\rangle$, over K different samples of the system in the limit of large K. If the variable has been averaged in time, we write $\langle\overline{\hat{X}}\rangle$ to denote the time-and-ensemble average. Carrying out the ensemble average in equations (A.20)–(A.22) gives:

$$R_d = \frac{N_d}{\tau}, \tag{A.23}$$

$$R_a = \frac{N_a}{\tau}, \tag{A.24}$$

$$R = \frac{N}{\tau}, \tag{A.25}$$

where $R_d \equiv \langle\overline{\hat{R}_d}\rangle$, $R_a \equiv \langle\overline{\hat{R}_a}\rangle$ and $R \equiv \langle\overline{\hat{R}}\rangle$ are the *time-and-ensemble averages of the total rates per site* (for diffusion, adsorption and all events, respectively), while $N_d \equiv \langle\hat{N}_d\rangle$, $N_a \equiv \langle\hat{N}_a\rangle$, and $N \equiv \langle\hat{N}\rangle$ specify the ensemble averages of the numbers of performed events per site (for diffusion, adsorption and all events, respectively), and $\tau \equiv \langle t\rangle$ is the ensemble average of the elapsed time.

On the other hand, performing the time-and-ensemble average on equations (A.2), (A.4) and (A.6), and then dividing by the total number of adsorption sites, L_xL_y, gives:

$$R_d = \sum_{\alpha\in\{d\}} M_\alpha k_\alpha, \tag{A.26}$$

$$R_a = M_a k_a = (1-\theta)F, \tag{A.27}$$

$$R = R_d + R_a = \sum_{\alpha\in\{e\}} M_\alpha k_\alpha, \tag{A.28}$$

where $M_\alpha \equiv \langle\overline{\widehat{M}_\alpha}\rangle$ and $M_a \equiv \langle\overline{\widehat{M}_a}\rangle = 1-\theta$ are the corresponding time-and-ensemble averages of the multiplicities per site, and $\theta = \langle\hat{\theta}\rangle$ is the ensemble average of the coverage.

Table B2. Microscopic diffusion activation energy barriers (in eV) for Ni/Cu system.

Type [class, subclass]	Single atom diffusion events															
	0	1	2	3	4	5	6	7	8	9	10	11	12	13	14	15
	[0,0]	[1,0]	[1,0]*	[2,0]	[2,0]*	[2,1]	[2,1]*	[2,2]	[3,0]	[3,0]*	[3,1]	[3,2]	[4,0]	[4,1]	[4,2]	[5,0]
0 [0,0]	0.031	0.028	×	0.015	×	0.009	×	×	0.008	×	×	×	×	×	×	×
1 [1,0]	0.568	0.016	0.505	0.014	0.159	0.006	0.172	0.000	0.001	0.180	0.000	×	0.023	×	×	×
2 [2,0]	0.938	0.439	0.746	0.364	0.743	0.389	0.541	0.305	0.500	0.562	0.319	×	0.263	×	×	×
3 [2,1]	0.800	0.489	0.550	0.450	0.467	0.448	0.356	0.366	0.404	0.372	0.382	0.659	0.353	0.531	0.423	0.643
4 [2,2]	×	0.678	×	0.340	×	0.334	×	0.596	0.283	×	0.115	×	0.170	×	×	×
5 [3,0]	1.290	0.804	∞	0.704	0.500	0.742	0.662	0.629	0.644	0.658	0.645	×	0.571	×	×	×
6 [3,1]	×	0.875	×	0.690	×	0.693	×	0.482	0.57	×	0.518	0.902	0.429	0.892	0.931	0.945
7 [3,2]	×	×	×	×	×	1.162	×	×	×	×	1.144	1.191	×	1.129	1.259	0.992
8 [4,0]	×	1.145	×	0.959	×	1.220	×	1.157	0.858	×	0.839	×	0.726	×	×	×
9 [4,1]	×	×	×	×	×	1.330	×	×	×	×	1.384	1.209	1.225	1.400	1.226	1.000
10 [4,2]	×	×	×	×	×	1.310	×	×	×	×	1.120	1.291	×	1.090	1.175	1.100
11 [5,0]	×	×	×	×	×	1.507	×	×	×	1.382	1.482	1.326	×	1.326	1.361	1.174

Concerted island diffusion			
Atoms in the island	Type	Energy (eV)	Name
2	I2	0.021	Dimer
3	I3	0.148	Trimer
4	I4	0.157	Tetramer
5	I5	0.220	Pentamer
6	I6	0.199	Hexamer
7	I7	0.369	Heptamer
8	I8	0.380	Octamer

Concerted two-atom diffusion	
Multi-atom	Energy (eV)
C1	0.654
C2	0.633
C3	0.294
C4	0.218

Equations (A.23)–(A.25)) and (A.26)–(A.28) provide two alternative expressions to determine each total rate (R_d, R_a and R). Since R can be used to determine the probability of each event type (see section 2.4) and R_d is directly connected to the tracer diffusivity (see section appendix A.2), this study focuses on the analysis of the temperature dependence of both R and R_d. In addition, equations (A.26)–(A.28) enable describing the particular contribution of every event type into the apparent activation energy of R, R_a and R_d (and, thus, the diffusivity), as shown in section 2.5.

A.2. Tracer diffusivity (diffusion constant)

In submonolayer growth under a constant flux of adparticles, the squared distance travelled by the adparticles, when divided by the number of adsorbed particles, is proportional to the elapsed time [33]:

$$\frac{\langle \hat{\mathcal{R}}^2 \rangle}{\langle \hat{n}_a \rangle} = 2\delta D_{\mathrm{T}} \langle t \rangle. \tag{A.29}$$

Here, the hat symbol ($\hat{}$) denotes the instantaneous value of any time-dependent variable at time t, δ is the dimensionality ($= 2$ for diffusion on a surface), $\hat{n}_a$ is the number of adsorbed particles, $\hat{\mathcal{R}}^2 = \Sigma_{i=1}^{\hat{n}_a} |\hat{\mathbf{x}}_i - \mathbf{x}_i^*|^2$ is the total squared distance travelled by the adparticles, with $\hat{\mathbf{x}}_i$ and $\mathbf{x}_i^*$ denoting the position of adparticle i at time t and when it was adsorbed, respectively, $\langle \hat{X} \rangle$ is the ensemble average of $\hat{X}$ over K samples in the limit of large K, and D_{T} is the diffusion constant or diffusivity. In this manner, the diffusivity can be determined from equation (A.29) as:

$$D_{\mathrm{T}} = \frac{1}{2\delta \langle \hat{n}_a \rangle} \frac{\langle \hat{\mathcal{R}}^2 \rangle}{\langle t \rangle}. \tag{A.30}$$

On the other hand, we consider the correlation factor, f_{T}, defined as the proportionality factor between the total square distance travelled by all adparticles, $\langle \hat{\mathcal{R}}^2 \rangle$, and the total number of performed diffusion hops, $\langle \hat{n}_d \rangle$:

$$f_{\mathrm{T}} = \frac{\langle \hat{\mathcal{R}}^2 \rangle}{l^2 \langle \hat{n}_d \rangle}, \tag{A.31}$$

with l the hop distance between adjacent adsorption sites. The correlation factor accounts for memory effects between consecutive hops at finite coverages, when hopping from site i to site j leaves site i empty and, thus, the adparticle has a higher chance of returning to i [33]. At very low coverage, the particles perform completely independent random walks and $\langle \hat{\mathcal{R}}^2 \rangle = l^2 \langle \hat{n}_d \rangle$. Thus, $f_{\mathrm{T}} = 1$. At finite coverages, however, each particle is affected by the presence of (and the interaction with) the other particles and, thus, their random walks become correlated. As a result, f_{T} departs from 1.

By using the correlation factor, the diffusivity can be easily re-written as:

$$D_{\mathrm{T}} = \frac{l^2}{2\delta\theta} f_{\mathrm{T}} R_d, \tag{A.32}$$

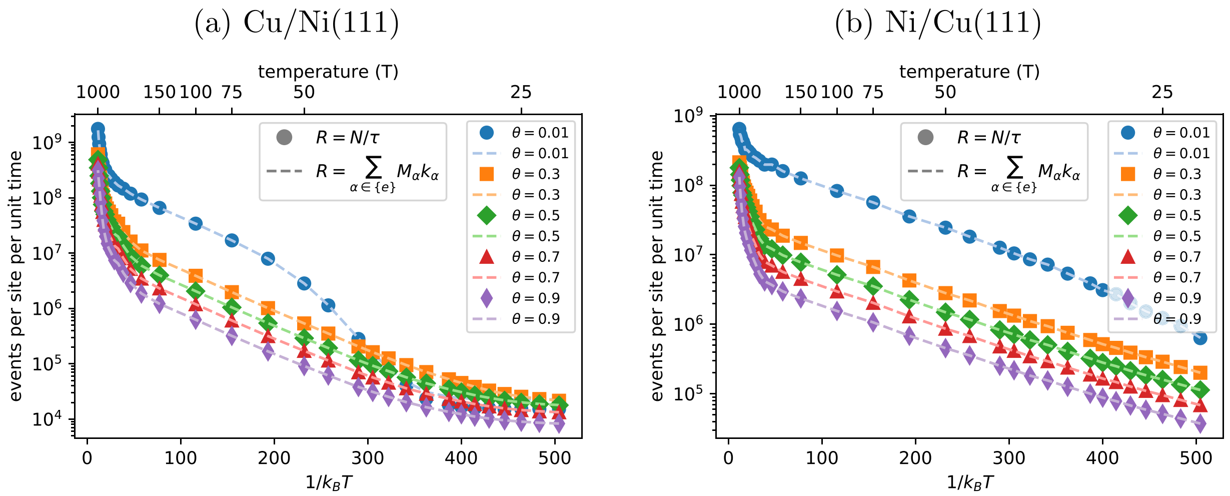
(a) Cu/Ni(111)
(b) Ni/Cu(111)

Figure C1. Average total rate per site, $R = R_d + R_a$, as a function of inverse temperature for various coverages, as indicated, for (a) Cu/Ni(111), and (b) Ni/Cu(111).

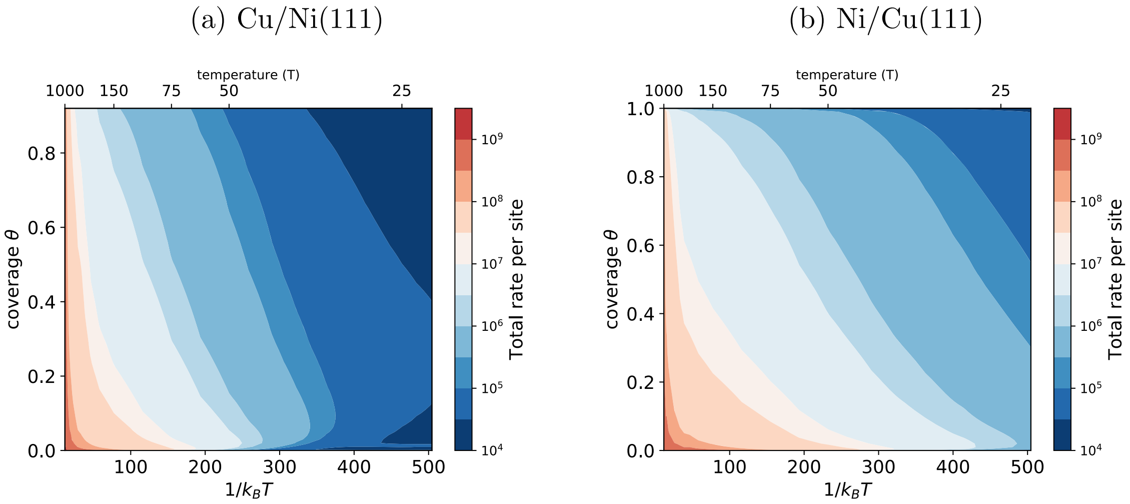
(a) Cu/Ni(111)
(b) Ni/Cu(111)

Figure C2. Top view of a three-dimensional plot of the average total rate per site, $R = R_d + R_a$, as a function of both coverage and temperature/inverse temperature for (a) Cu/Ni(111), and (b) Ni/Cu(111).

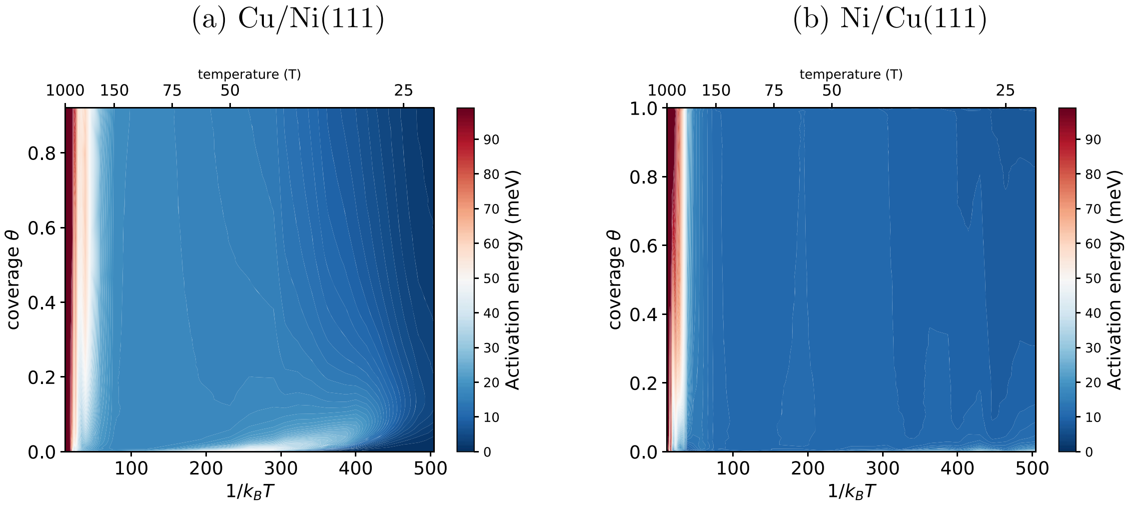
(a) Cu/Ni(111)
(b) Ni/Cu(111)

Figure C3. Top view of a three-dimensional plot of the apparent activation energy of the average total rate per site, E^R_{app}, as a function of both coverage and temperature/inverse temperature for (a) Cu/Ni(111), and (b) Ni/Cu(111).

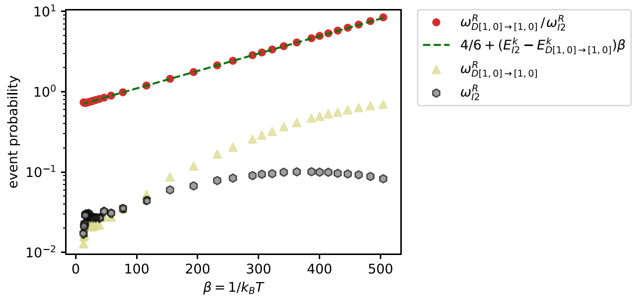

Figure C4. Ratio of the probability to observe non-concerted dimer diffusion to that for concerted diffusion, $\frac{\omega^R_{D[1,0]\to[1,0]}}{\omega^R_{\mathrm{I2}}} = \frac{M_{D[1,0]\to[1,0]}k_{D[1,0]\to[1,0]}}{M_{\mathrm{I2}}k_{\mathrm{I2}}}$ and the expected result $\frac{4\mathrm{e}^{-E^k_{D[1,0]\to[1,0]}\beta}}{6\mathrm{e}^{-E^k_{\mathrm{I2}}\beta}}$, for Ni/Cu(111) at $\theta = 0.10$. This plot confirms that the events $D[1,0] \to [1,0]$ and I2 correspond to non-concerted dimer diffusion and concerted dimer diffusion, respectively. Note that the ratio is larger than 1 at low temperatures, indicating that non-concerted dimer diffusion is more probable, while the ratio becomes smaller than 1 at high temperatures, demonstrating that concerted dimer diffusion occurs more frequently.

where $\theta = \langle\hat{\theta}\rangle$ is the ensemble average of the coverage (as in equation (A.27)), and $R_d = \langle\overline{\hat{R}_d}\rangle = \langle\hat{N}_d\rangle/\langle t\rangle = N_d/\tau$ is the time-and-ensemble average of the total diffusion rate per site (as in equation (A.23) and (A.26)). Since the factor $l^2/2\delta\theta$ is independent of temperature and typically the correlation factor has a very weak dependence on temperature [33], the temperature dependence of the diffusivity is essentially contained in the total diffusion rate R_d. Thus, in this study we focus on monitoring the temperature dependence of R_d as an excellent approximation to that of the diffusion constant, D_{T}.

A.3. Diffusivity under a constant deposition flux vs diffusivity for a fixed density of monomers

As described in equation (A.32), equation (1) reads:

$$D_{\mathrm{T}} = \frac{l^2}{2\delta\langle\hat{\theta}\rangle} f_{\mathrm{T}}\langle\overline{\hat{R}_d}\rangle \tag{A.33}$$

where $\hat{\theta}$ is the instantaneous value of the coverage at time t and $\langle\hat{\theta}\rangle \equiv \theta$ is the corresponding ensemble average. Similarly, $\hat{R}_d$ is the instantaneous value of the total diffusion rate per site and $\langle\overline{\hat{R}_d}\rangle \equiv R_d$ is the time-and-ensemble average. Accordingly, in equation (1), θ is an ensemble average while R_d is a time-and-ensemble average. This difference leads to a lower diffusivity (by a factor of $\frac{1}{2}$) when the density of monomers increases linearly with time under a constant deposition flux, as compared to the case when the density of monomers remains fixed. While this feature was already indicated in reference [33], here we offer a more detailed presentation.

For a constant flux, F, the coverage evolves in time by following the exact expression $\hat{\theta} = 1 - \mathrm{e}^{-Ft}$ (see text after equation (A.5)). This is well approximated by $\hat{\theta} \approx Ft$ when t is small, i.e. during the initial, low-coverage stage. In this stage, gradually adsorbed monomers diffuse freely without hitting each others and the correlation factor is one ($f_{\mathrm{T}} = 1$). In addition, the monomer density, $\hat{n}_{\mathrm{m}}$, is the only contribution to the coverage: $\hat{\theta} = \hat{n}_{\mathrm{m}}$. Thus, the ensemble average of the monomer density is:

$$\langle\hat{n}_{\mathrm{m}}\rangle = \langle\hat{\theta}\rangle \approx \langle Ft\rangle = F\langle t\rangle \tag{A.34}$$

On the other hand, the time-and-ensemble average is:

$$\langle\overline{\hat{n}_{\mathrm{m}}}\rangle = \langle\overline{\hat{\theta}}\rangle \approx \langle\overline{Ft}\rangle = F\langle\frac{\int_0^t t\,\mathrm{d}t}{\int_0^t\,\mathrm{d}t}\rangle = F\langle\frac{\frac{1}{2}t^2}{t}\rangle = \frac{1}{2}F\langle t\rangle \tag{A.35}$$

Accordingly, using equation (A.26) the total diffusion rate per adsorption site is:

$$\begin{aligned}\langle\overline{\hat{R}_d}\rangle &= \sum_{\alpha\in\{d\}}\langle\overline{\hat{M}_\alpha}\rangle k_\alpha = \langle\overline{\hat{M}_{\mathrm{m}}}\rangle k_{\mathrm{m}} = 6\langle\overline{\hat{n}_{\mathrm{m}}}\rangle k_{\mathrm{m}} \\ &= 6\frac{1}{2}F\langle t\rangle k_{\mathrm{m}} = 3F\langle t\rangle k_{\mathrm{m}},\end{aligned} \tag{A.36}$$

where we have used that $\hat{M}_{\mathrm{m}} = 6\hat{n}_{\mathrm{m}}$, with 6 being the number of hopping directions in a triangular lattice. Finally, for the diffusivity we have ($\delta = 2$ and $f_T = 1$):

$$D_{\mathrm{T}} = \frac{l^2}{2\delta\langle\hat{\theta}\rangle} f_{\mathrm{T}}\langle\overline{\hat{R}_d}\rangle = \frac{l^2}{4\langle\hat{\theta}\rangle}\langle\overline{\hat{R}_d}\rangle = \frac{l^2}{4F\langle t\rangle}3F\langle t\rangle k_{\mathrm{m}} = \frac{3}{4}k_{\mathrm{m}}l^2. \tag{A.37}$$

In comparison, for a system with a fixed density of monomers (no deposition flux) the ensemble average of the monomer density coincides with the time-and-ensemble average and one obtains $D_{\mathrm{T}} = \frac{3}{2}k_{\mathrm{m}}l^2$. For a square lattice with 4 hopping directions, $\hat{M}_{\mathrm{m}} = 4\hat{n}_{\mathrm{m}}$ and one obtains $D_{\mathrm{T}} = \frac{1}{2}k_{\mathrm{m}}l^2$ under a constant deposition flux while a constant density of monomers leads to $D_{\mathrm{T}} = k_{\mathrm{m}}l^2$. The validity of the expressions obtained under a constant flux was confirmed in figures 1 and S1 of reference [33] for the triangular and square lattices, respectively.

A.4. Kinetic Monte Carlo

For the actual simulations, we use the standard, rejection-free, time-dependent implementation of the kinetic Monte Carlo (KMC) method with periodic boundary conditions [29, 33, 38, 54, 56]. A flowchart of the KMC procedure is presented in figure A1. Regarding the central rhombus in figure A1, a threefold termination criterion is used, based on surpassing any of the maximum values specified by the user for (i) the coverage $\hat{\theta}$, (ii) the simulated time t, and (iii) the total number of simulated events $\hat{n} = \hat{n}_d + \hat{n}_a$. In order to initiate the simulation (and keep it going) the fundamental ingredients are the combination of a specific geometry (figure A1(I), here a triangular lattice), a complete list of possible events (figure A1(II).) and their rates (figure A1(III)). Although nothing prevents starting from an arbitrary coverage, in this study the initial configuration is always an empty surface (no adatoms).

Initially, the stop criteria are not met and the main loop starts by updating the simulated time (figure A1(a)). This is done by adding the time increment $\Delta t = -\log(u)/\hat{r}$ to the current value of t, as indicated in section appendix A.1. Continuing with the algorithm, a random number is used to select the

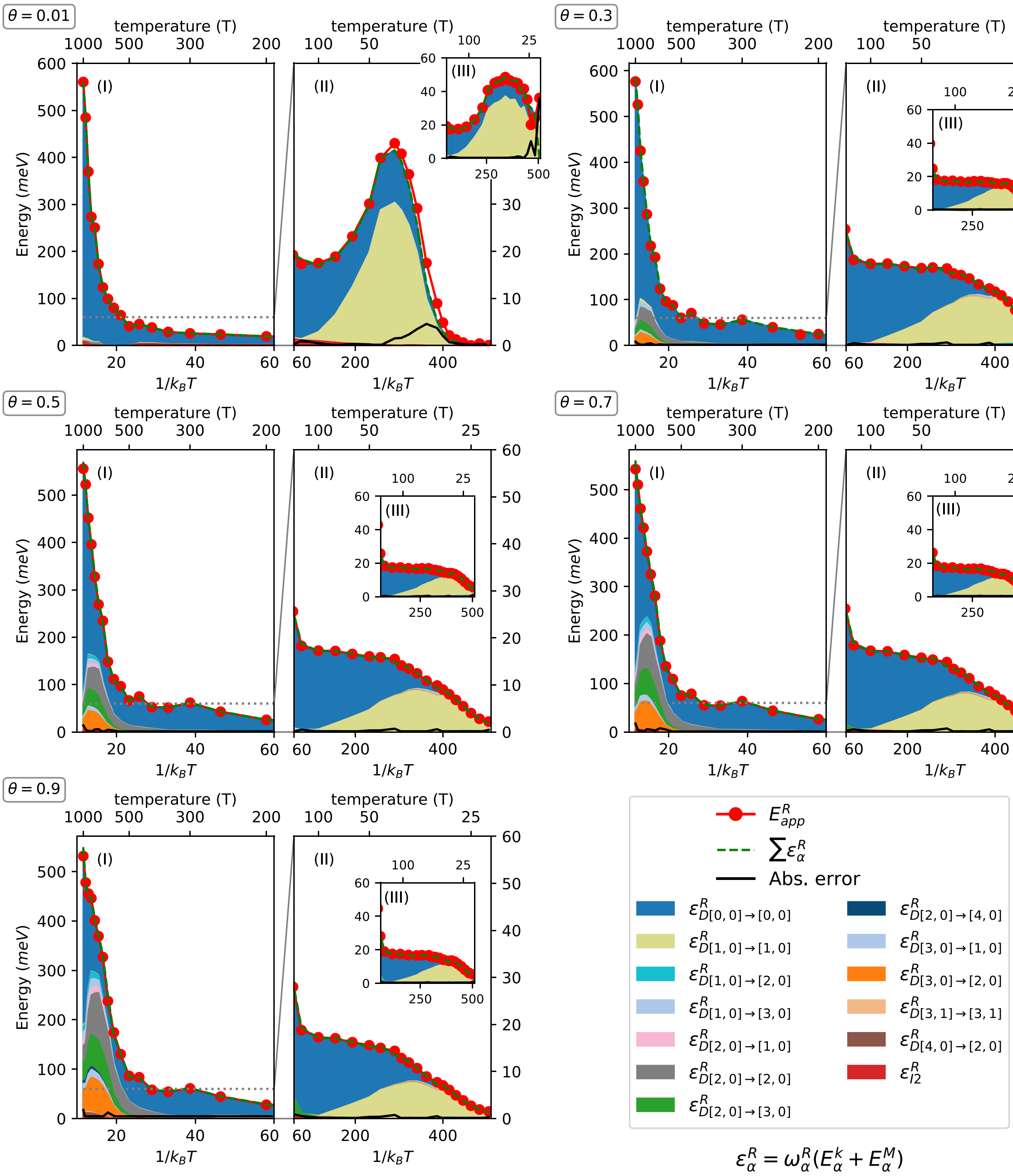

Figure C5. Temperature dependence of E^R_{app} for Cu/Ni(111) at representative coverage values, as indicated. Two temperature regions are shown: (I) $1000 \geqslant T > 150$ K, and (II) $150 \geqslant T \geqslant 23$ K, with region II magnified. E^R_{app} is described well by $\sum_{\alpha\in\{e\}}\epsilon^R_\alpha$, where $\epsilon^R_\alpha = \omega^R_\alpha(E^k_\alpha + E^M_\alpha)$. The absolute error $|E^R_{\text{app}} - \sum_{\alpha\in\{e\}}\epsilon^R_\alpha|$ is also plotted. The number of significant contributions to E^R_{app} increases with coverage and temperature. The inset in region II displays $E^{R_d}_{\text{app}}$.

next event that will be executed (figure A1(b)). This is done by randomly choosing one rate among all the current rates, i.e. among all the diffusion and adsorption events that are currently possible. The next step in the algorithm is to execute the selected event (figure A1(c)). From a computational perspective, adsorption implies adding an atom to an empty site while, in general, diffusion requires removing several atoms from the occupied initial sites and adding them to the empty final sites. As a result, the adsorption and diffusion rates need to be updated for the involved sites as well as their neighbours (figure A1(d)), adding and deleting available events too. The main loop finishes here and it is repeated until a stop criterion is met.

In the simulations, the adsorption flux is fixed to 1.5×10^4 ML/s and the temperature is varied from 23 to 1000 K for both systems under study. We use just one value of the flux, since the behaviour of the system is the same for other values by simply shifting the temperature range [33]. The simulated surfaces contain 283×283 Cartesian units, corresponding to $L_x \times L_y = 283 \times 326 = 92\,258$ adsorption sites

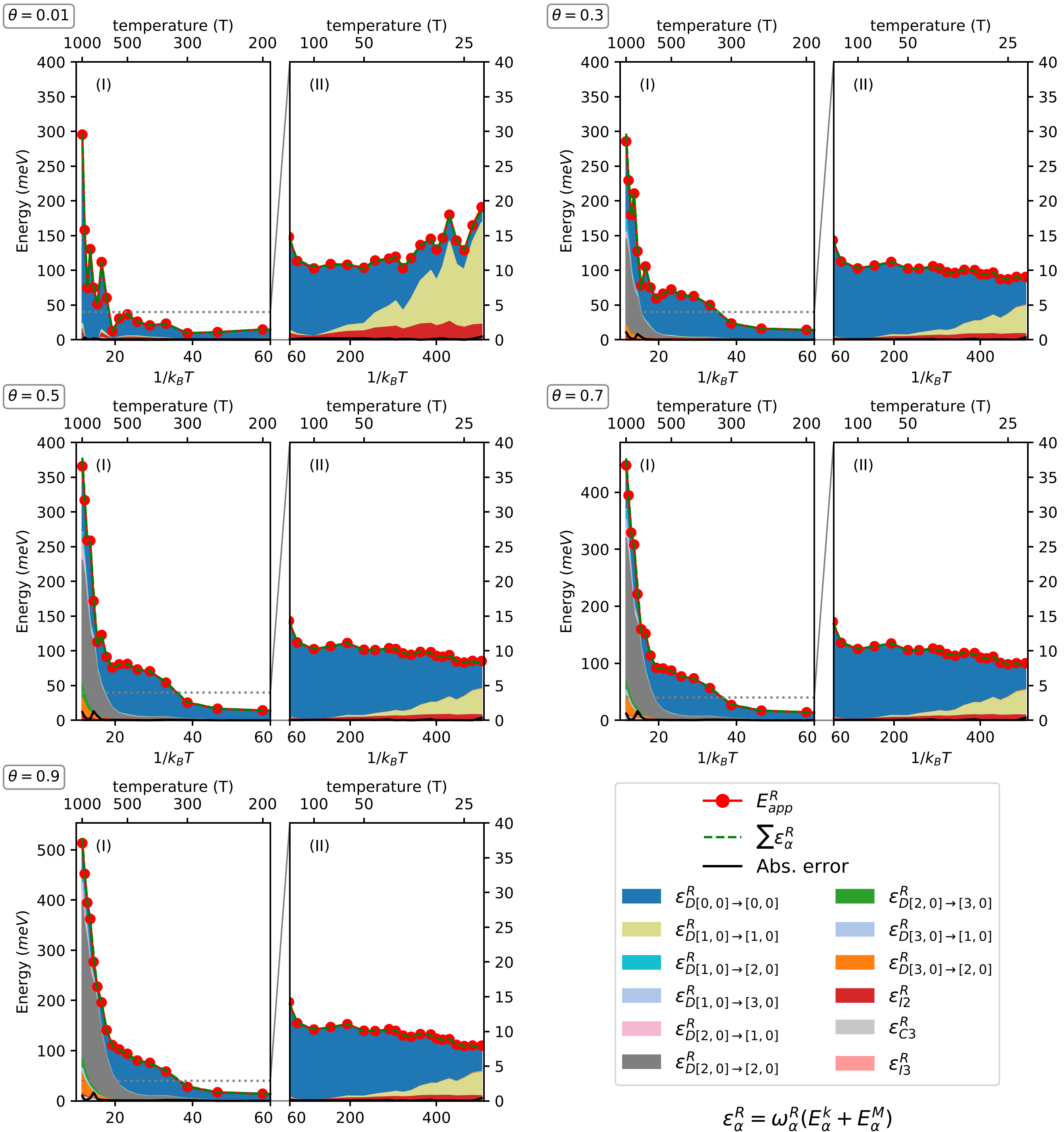

Figure C6. Temperature dependence of E^R_{app} for Ni/Cu(111) at representative coverage values, as indicated. Two temperature regions are shown: (I) $1000 \geqslant T > 150$ K, and (II) $150 \geqslant T \geqslant 23$ K, with region II magnified. E^R_{app} is described well by $\sum_{\alpha\in\{e\}} \epsilon^R_\alpha$, where $\epsilon^R_\alpha = \omega^R_\alpha(E^k_\alpha + E^M_\alpha)$. The absolute error $|E^R_{\text{app}} - \sum_{\alpha\in\{e\}} \epsilon^R_\alpha|$ is also plotted. The number of significant contributions to E^R_{app} increases with coverage and temperature.

in the triangular lattice, and periodic boundary conditions are applied. The simulations are evolved until 100% coverage ($\theta = 1$ ML), repeating them $K = 10$ times in order to obtain ensemble averages for all quantities of interest. Strictly two-dimensional growth is simulated (no three-dimensional features are attempted). Snapshots of the surface configuration are obtained every 5% of coverage, which are used as input for the morphology analysis (see section 3.2).

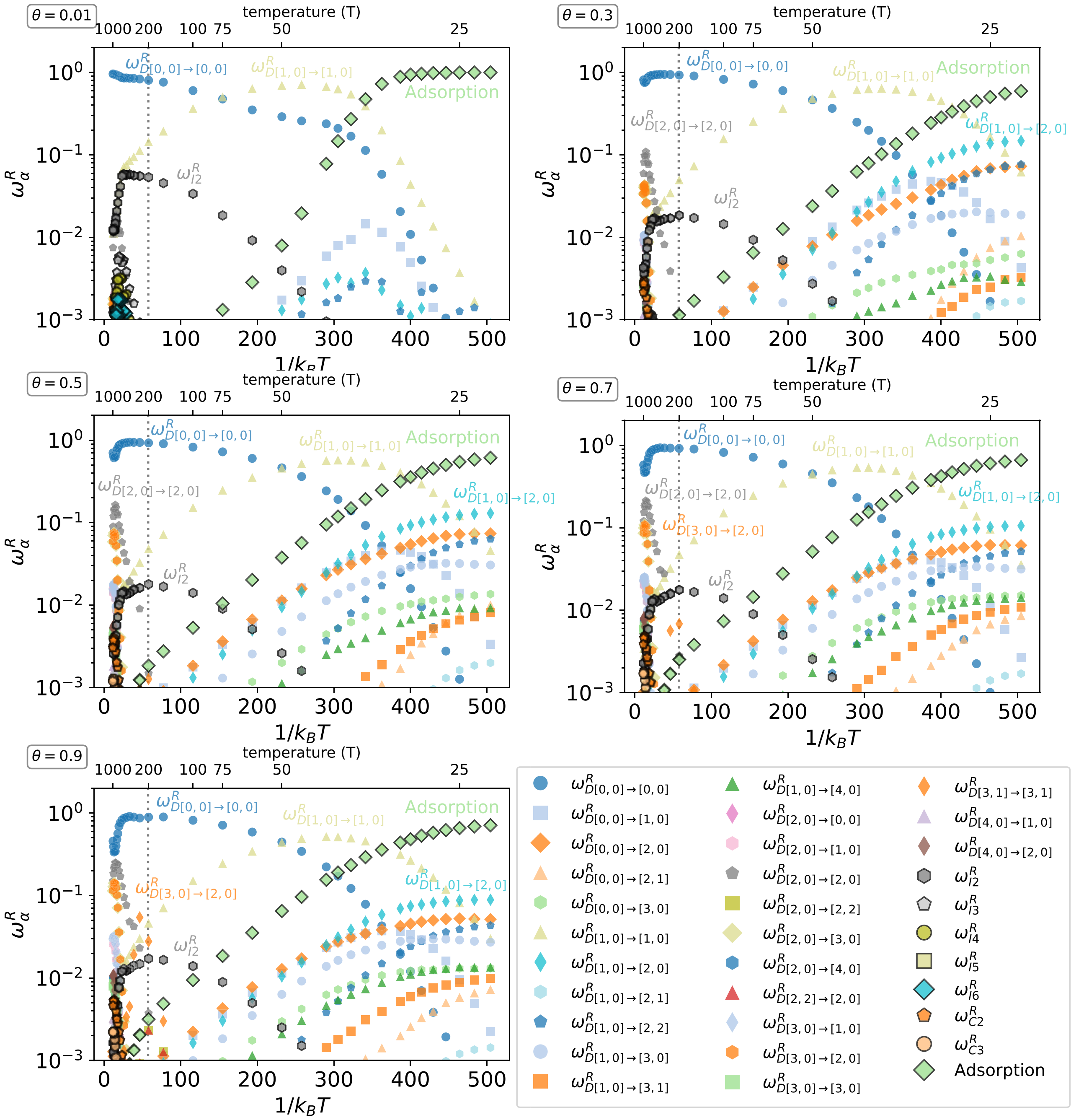

Figure C7. Temperature dependence of the event probabilities (ω_α^R) for Cu/Ni(111) at representative coverages, as indicated. Only those events whose probability is higher than 10^{-3} are shown.

Appendix B. Diffusion events and activation energies

B.1. Single-atom diffusion events

See figure B1.

B.2. Activation energies for Cu/Ni and Ni/Cu

See tables B1 and B2.

Appendix C. Additional results

C.1. Additional plots for the total rate and its apparent activation energy

See figures C1–C10.

Appendix D. Input parameters

Here we show the input parameters required to perform a typical simulation of the present study.

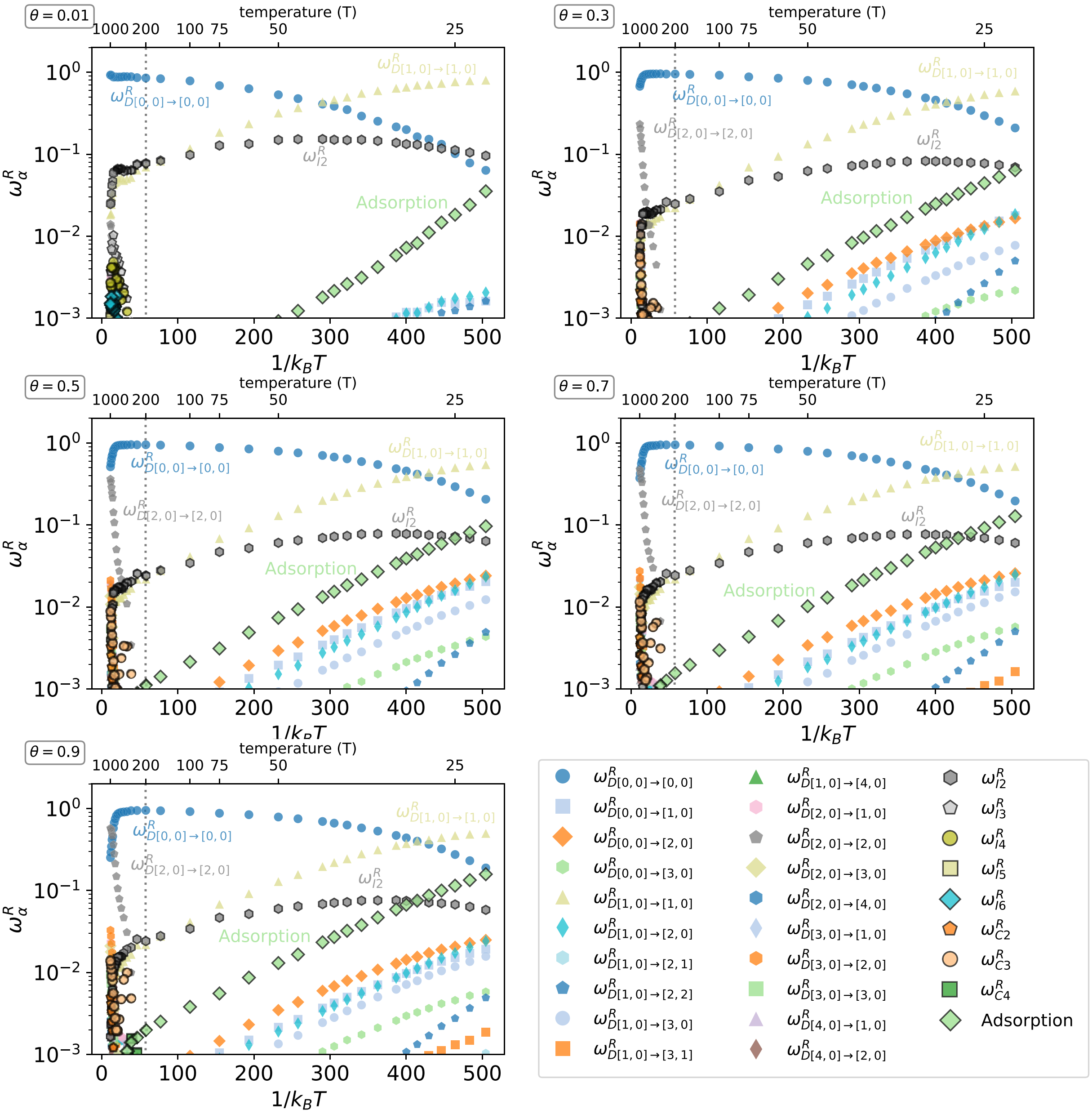

Figure C8. Temperature dependence of the event probabilities (ω^R_α) for Ni/Cu(111) at representative coverages, as indicated. Only those events whose probability is higher than 10^{-3} are shown.

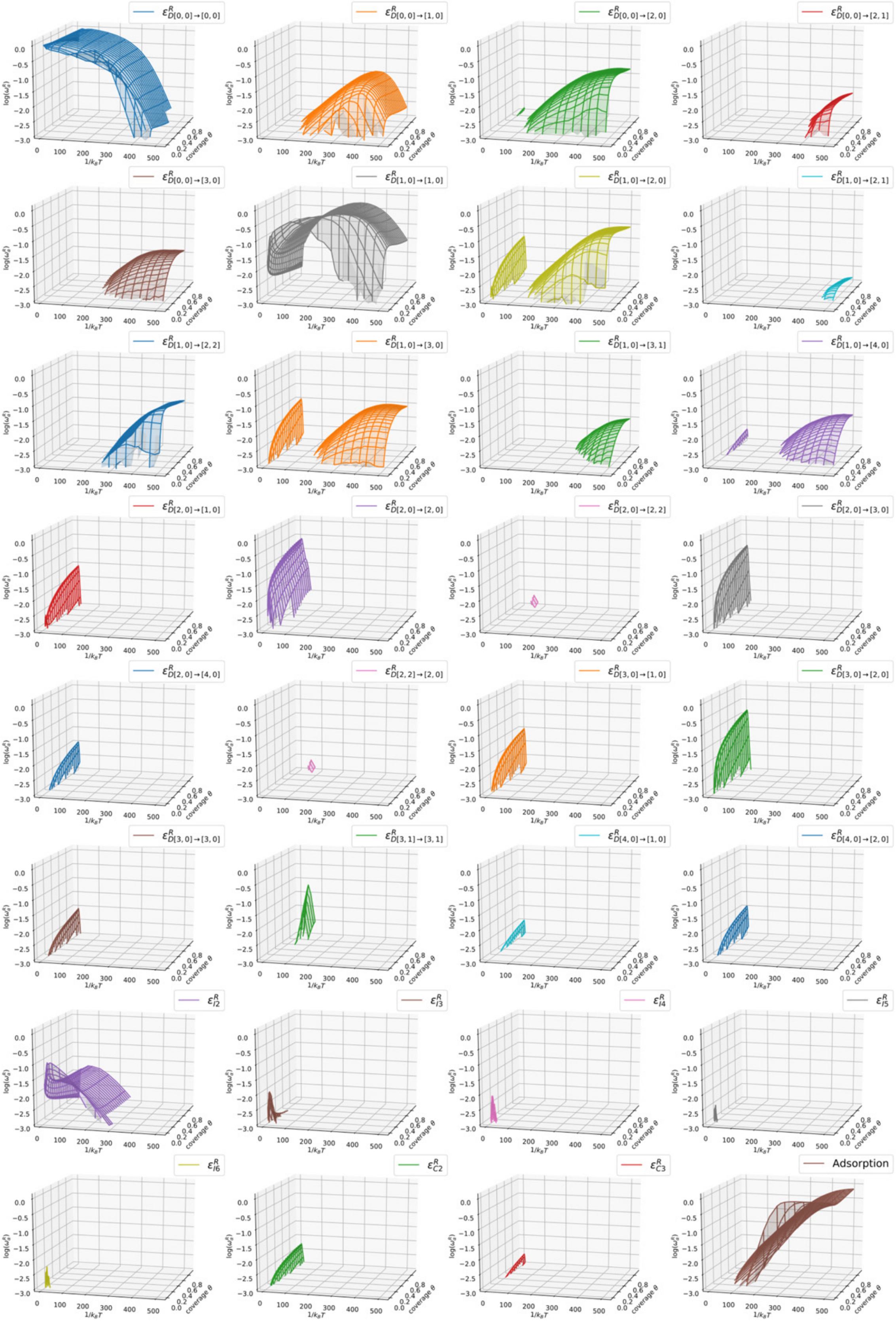

Figure C9. Event probabilities (ω^R_α) as a function of coverage and inverse temperature for the most relevant events in the Cu/Ni(111) system.

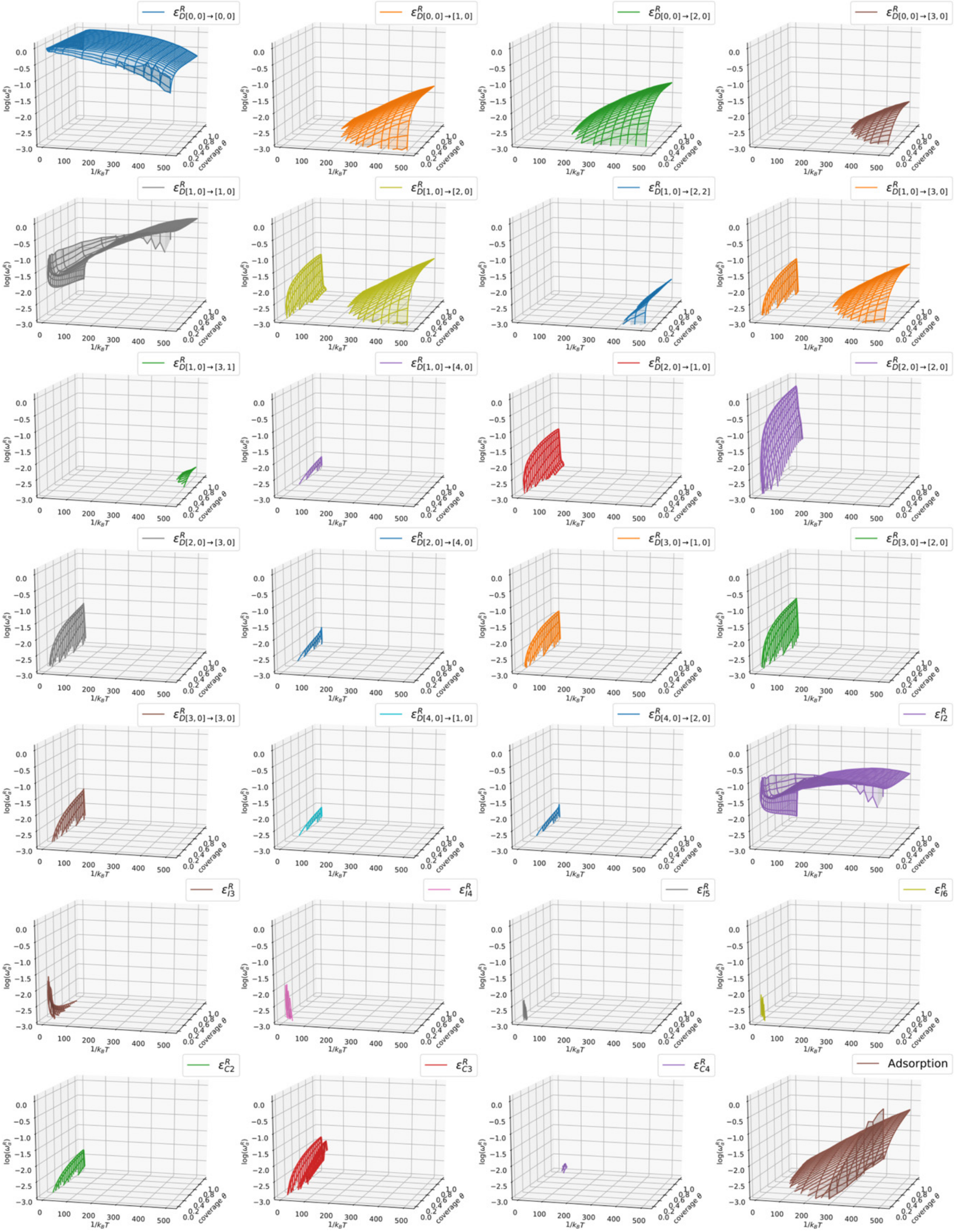

Figure C10. Event probabilities (ω^R_α) as a function of coverage and inverse temperature for the most relevant events in the Ni/Cu(111) system.

The used Git revision of 'Morphokinetics' is `2b2811ae1187e69b3c55bf92ccb2c67c87761251`. The command to compile the code is '`ant jar`' and the command to run a simulation is '`java -jar dist/morphokinetics.jar`'. The latter must be executed within a folder containing the file `parameters`, with the following content (removed the text inside [ ]):

```
{
  "automaticCollections": true,
  "calculationMode": "concerted",
  "cartSizeX": 283,
  "cartSizeY": 283,
  "coverage": 100,
  "depositionFlux": 15000.0,
  "doIslandDiffusion": true,
  "doMultiAtomDiffusion": true,
  "forceNucleation": false,
  "justCentralFlake": false,
  "numberOfSimulations": 10,
  "outputData": true,
  "outputDataFormat": [
    {
      "type": "extra"
    },
    {
      "type": "ae"
    },
    {
      "type": "mko"
    }
  ],
  "psd": false,
  "randomSeed": false,
  "ratesLibrary": "CuNi", [or "NiCu"]
  "temperature": 23, [ranges from 23 to 1000]
  "withGui": false
}
```

ORCID iDs

Joseba Alberdi-Rodriguez https://orcid.org/0000-0002-9078-8553
Shree Ram Acharya https://orcid.org/0000-0001-7020-7275
Talat S Rahman https://orcid.org/0000-0003-3889-7776
Andres Arnau https://orcid.org/0000-0001-5281-3212
Miguel A Gosálvez https://orcid.org/0000-0002-7621-0755

References

[1] Zhang H 2015 *ACS Nano* **9** 9451–69
[2] Lin Z *et al* 2016 *2D Mater.* **3** 042001
[3] Shen Q, Gao H Y and Fuchs H 2017 *Nano Today* **13** 77–96
[4] Zhuiykov S, Kawaguchi T, Hai Z, Akbari M K and Heynderickx P M 2017 *Appl. Surf. Sci.* **392** 231–43
[5] Novoselov K S, Geim A K, Morozov S V, Jiang D, Zhang Y, Dubonos S V, Grigorieva I V and Firsov A A 2004 *Science* **306** 666–9
[6] Dávila M E, Xian L, Cahangirov S, Rubio A and Lay G L 2014 *New J. Phys.* **16** 095002
[7] Grazianetti C, Cinquanta E and Molle A 2016 *2D Mater.* **3** 012001
[8] Clair S and de Oteyza D G 2019 *Chem. Rev.* **119** 4717–76
[9] Ariga K, Hill J P, Lee M V, Vinu A, Charvet R and Acharya S 2008 *Sci. Technol. Adv. Mater.* **9** 014109
[10] Kim K S, Zhao Y, Jang H, Lee S Y, Kim J M, Kim K S, Ahn J H, Kim P, Choi J Y and Hong B H 2009 *Nature* **457** 706–10
[11] Huang M, Biswal M, Park H J, Jin S, Qu D, Hong S, Zhu Z, Qiu L, Luo D, Liu X, Yang Z, Liu Z, Huang Y, Lim H, Yoo W J, Ding F, Wang Y, Lee Z and Ruoff R S 2018 *ACS Nano* **12** 6117–27
[12] Takesaki Y, Kawahara K, Hibino H, Okada S, Tsuji M and Ago H 2016 *Chem. Mater.* **28** 4583–92
[13] Seah C M, Chai S P and Mohamed A R 2014 *Carbon* **70** 1–21
[14] Tian J, Hu B, Wei Z, Jin Y, Luo Z, Xia M, Pan Q and Liu Y 2014 *Appl. Surf. Sci.* **300** 73–9
[15] Huet B and Raskin J P 2018 *Carbon* **129** 270–80
[16] Mueller N S, Morfa A J, Abou-Ras D, Oddone V, Ciuk T and Giersig M 2014 *Carbon* **78** 347–55
[17] Liu W, Li H, Xu C, Khatami Y and Banerjee K 2011 *Carbon* **49** 4122–30
[18] Davisson C and Germer L H 1927 *Nature* **119** 558–60
[19] Davisson C and Germer L H 1927 *Phys. Rev.* **30** 705–40
[20] Viefhaus H 1987 *Mater. Corros.* **38** 404
[21] Müller E W and Bahadur K 1956 *Phys. Rev.* **102** 624–31
[22] Müller E W 1956 *J. Appl. Phys.* **27** 474–6
[23] Binnig G and Rohrer H 1983 *Surf. Sci.* **126** 236–44
[24] Antczak G and Ehrlich G 2010 *Surface Diffusion: Metals, Metal Atoms, and Clusters* (Cambridge: Cambridge University Press)
[25] Knorr N, Brune H, Epple M, Hirstein A, Schneider M A and Kern K 2002 *Phys. Rev.* B **65** 115420
[26] Repp J, Moresco F, Meyer G, Rieder K H, Hyldgaard P and Persson M 2000 *Phys. Rev. Lett.* **85** 2981–4
[27] Repp J, Meyer G, Rieder K H and Hyldgaard P 2003 *Phys. Rev. Lett.* **91** 206102
[28] Morgenstern K, Braun K F and Rieder K H 2004 *Phys. Rev. Lett.* **93** 056102
[29] Jansen A P J 2012 *An Introduction to Kinetic Monte Carlo Simulations of Surface Reactions* (*Lecture Notes in Physics No 856*) 1st edn (New York: Springer) https://link.springer.com/book/10.1007/978-3-642-29488-4
[30] Gillespie D T 1977 *J. Phys. Chem.* **81** 2340–61
[31] Chorkendorff I and Niemantsverdriet J W 2003 *Concepts of Modern Catalysis and Kinetics* (New York: Wiley)
[32] Leach A 2001 *Molecular Modelling: Principles and Applications* (Englewood Cliffs, NJ: Prentice Hall) https://books.google.es/books?id=kB7jsbV-uhkC
[33] Gosálvez M A and Alberdi-Rodriguez J 2017 *J. Phys. Chem.* C **121** 20315–22
[34] Venables J A, Spiller G D T and Hanbucken M 1984 *Rep. Prog. Phys.* **47** 399
[35] Amar J G, Family F and Lam P M 1994 *Phys. Rev.* B **50** 8781–97
[36] Ratsch C and Venables J A 2003 *J. Vac. Sci. Technol.* A **21** S96–S109
[37] Körner M, Einax M and Maass P 2012 *Phys. Rev.* B **86** 085403
[38] Acharya S R, Shah S I and Rahman T S 2017 *Surf. Sci.* **662** 42–58
[39] Onat B and Durukanoğlu S 2014 *J. Phys.: Condens. Matter* **26** 035404
[40] Koschel H, Held G and Steinrück H P 2000 *Surf. Sci.* **453** 201–13

[41] Koschel H, Held G, Trischberger P, Widdra W, Birkenheuer U and Steinrück H P 1999 *Appl. Surf. Sci.* **142** 18–22
[42] Boeglin C, Stanescu S, Cherifi S, Deville J P, Ohresser P, Barbier A and Brookes N B 2002 *Surf. Sci.* **507–510** 522–9
[43] Pons S, Mallet P, Magaud L and Veuillen J Y 2002 *Surf. Sci.* **511** 449–58
[44] Mulazzi M, Stanescu S, Fujii J, Vobornik I, Boeglin C, Belkhou R, Rossi G and Barbier A 2006 *Surf. Sci.* **600** 3938–42
[45] Wang S C, Kürpick U and Ehrlich G 1998 *Phys. Rev. Lett.* **81** 4923–6
[46] Schlößer D C, Morgenstern K, Verheij L K, Rosenfeld G, Besenbacher F and Comsa G 2000 *Surf. Sci.* **465** 19–39
[47] Kellogg G 1994 *Phys. Rev. Lett.* **73** 1833
[48] Zhang Z and Lagally M G 1997 *Science* **276** 377–83
[49] Wang S and Ehrlich G 1997 *Phys. Rev. Lett.* **79** 4234
[50] Wu H H, Signor A and Trinkle D R 2010 *J. Appl. Phys.* **108** 023521
[51] Signor A, Wu H H and Trinkle D R 2010 *Surf. Sci.* **604** L67–70
[52] Acharya S R and Rahman T S 2018 *J. Mater. Res.* **33** 709–19
[53] Foiles S, Baskes M and Daw M S 1986 *Phys. Rev.* B **33** 7983
[54] Trushin O, Karim A, Kara A and Rahman T S 2005 *Phys. Rev.* B **72** 115401
[55] Kim S Y, Lee I H and Jun S 2007 *Phys. Rev.* B **76** 245407
[56] Ferrando N, Gosálvez M A and Ayuela A 2014 *J. Phys. Chem.* C **118** 11636–48
[57] Venables J A 1987 *Phys. Rev.* B **36** 4153–62
[58] Jacobs T D B, Junge T and Pastewka L 2017 *Surface Topography: Metrology and Properties* **5** 013001
[59] Elson J M and Bennett J M 1995 *Appl. Opt.* **34** 201–8
[60] Czifra Á 2009 Sensitivity of power spectral density (psd) analysis for measuring conditions *Towards Intelligent Engineering and Information Technology* ed I Rudas, J Fodor and J Kacprzyk (Berlin: Springer) pp 505–17
[61] Gosalvez M A and Alberdi-Rodriguez J 2018 arXiv:1812.11398 [physics.chem-ph]